High-speed live cell interferometry for screening bioprinted organoids

Peyton J. Tebon[1,2,*], Bowen Wang[2,3,*], Alexander L. Markowitz[4], Graeme Murray[5], Huyen Thi Lam Nguyen[1], Nasrin Tavanaie[1], Thang L. Nguyen[2,3], Paul C. Boutros[4,6,7,8,9,10,11], Michael A. Teitell[2,3,6,7,8,9,12,#] and Alice Soragni[1,6,7,8,9,#]

[1]Department of Orthopaedic Surgery, David Geffen School of Medicine, University of California Los Angeles, CA
[2]Department of Bioengineering, University of California Los Angeles, CA
[3]Department of Pathology, David Geffen School of Medicine, University of California Los Angeles, CA
[4]Department of Human Genetics, University of California Los Angeles, CA
[5]Department of Physics, Virginia Commonwealth University, Richmond, VA
[6]Jonsson Comprehensive Cancer Center, University of California Los Angeles, CA
[7]Molecular Biology Institute, University of California Los Angeles, CA
[8]Eli and Edythe Broad Center of Regenerative Medicine and Stem Cell Research, University of California Los Angeles, CA
[9]California NanoSystems Institute, University of California Los Angeles, CA
[10]Department of Urology, University of California Los Angeles, CA
[11]Institute for Precision Health, University of California Los Angeles, CA
[12]Department of Pediatrics, David Geffen School of Medicine, University of California Los Angeles, CA

[*]These authors contributed equally to this work
[#]Correspondence to M.A.T. (mteitell@mednet.ucla.edu) and A.S. (alices@mednet.ucla.edu)

Abstract

There is increasing interest in leveraging tumor organoids for high-throughput drug screenings to investigate tumor biology and identify therapeutic leads. However, functional precision medicine platforms are limited by the difficulties of creating, scaling, and analyzing physiological disease models. Most systems use manually seeded organoids and take advantage of destructive endpoint assays to rapidly characterize response to treatment. These approaches fail to capture transitory changes and intra-sample heterogeneity that underlies much of the clinically observed resistance to therapy. We therefore developed bioprinted tumor organoids linked to real-time growth pattern quantitation via high-speed live cell interferometry (HSLCI). We demonstrate that bioprinting gives rise to 3D organoid structures that preserve histology and gene expression. These are suitable for imaging with HSLCI, enabling accurate parallel mass measurements for thousands of bioprinted organoids. In drug screening experiments, HSLCI rapidly identifies organoids transiently or persistently sensitive or resistant to specific therapies. We show that our approach can provide detailed, actionable information to guide rapid therapy selection.

Introduction

Functional approaches in precision cancer medicine entail exposing patient-derived tumor cells to therapeutic molecules to provide robust models for identifying drug candidates (compound screening) and to rapidly assess the potential efficacy of drugs for individual patients (therapy selection)[1–8]. While a small number of actionable mutations are known, the majority of patients have tumors that lack any currently actionable genomic alteration[9]. By directly measuring the effect of drugs on tissues or cells, functional precision medicine methods can inform on the therapeutic resistance and sensitivity landscape of tumors without requiring a priori full knowledge of the underlying molecular vulnerabilities[10,11].

Three-dimensional (3D) tumor organoids are promising models for precision cancer medicine that can be established rapidly and effectively from a variety of cell types and tissue sources, and accurately mimic a patient's response to therapy[3–5,8,11,12]. They are physiologically-relevant, personalized cancer models well suited for drug development and clinical applications[13,14]. We previously developed a screening platform that takes advantage of patient-derived tumor organoids seeded in a mini-ring format to automate high-throughput drug testing, with results available within a week from surgery[3,15,16]. The key outstanding limitations to the broad adoption of organoid screening approaches remail the time-intensive and operator-to-operator susceptibility of the cell seeding steps and destructive, population-level approaches required to assay them[17].

To overcome these, we developed a novel organoid screening approach that combines bioprinting for automated cell seeding with high-speed live cell interferometry (HSLCI) for non-invasive, label-free, real time monitoring. Bioprinting, a technique for precise, reproducible deposition of cells in bioinks onto sol-

id supports, is rapidly gaining traction in cancer biology[18–22]. Within the deposited bioink, embedded cells can interact with physiological microenvironment components[17]. We monitor bioprinted organoids with HSLCI that uses quantitative phase imaging (QPI) in order to rapidly monitor changes in dry biomass and biomass distribution of organoids over time[23–27,27,28]. QPI measurements of biomass changes allowed to distinguish drug-resistant from -sensitive cells in 2D cell culture models within hours of treatment[23–25,27–30]. Moreover, HSLCI-measured response profiles were found to match drug sensitivity observed in patient-derived xenograft (PDX) mouse models of breast cancer[24]. However, HSLCI has so far been applied exclusively to screening of cancer lines grown in 2D or single cell suspensions of excised PDX tumors[23–27,27,28]. Combining these two technologies, we demonstrate for the first time that bioprinted organoids deposited in uniform, flat layers of extracellular matrix are ideally suited for HSLCI imaging and enable real-time tracking of the growth patterns and drug responses of 3D organoids at a single organoid resolution.

Results

Bioprinting enables seeding cells in conformations suitable for imaging applications. To address current limitations[3,15,16] and facilitate non-invasive, label-free, real time imaging of 3D organoids by HSLCI, we optimized an automated cell printing protocol using an extrusion bioprinter. Our original platform takes advantage of seeding cells in mini-rings of Matrigel around the rim of 96-well plates[3,15,16] (**Figure 1A**). The empty center allows for implementation of liquid handlers and automation, facilitating media exchanges and addition of perturbagens[3,15,16]. We kept the empty center feature but altered our geometry to bioprint mini-squares of cells in Matrigel (**Figure 1A**). By positioning the sides of the square in the imaging path of the HSLCI, we can both sample a larger area as well prevent imaging artifacts due to uneven illumination at edges of the wells[26] (**Figure 1A**). Our bioprinting protocol entails suspending cells in a bioink consisting of a 3:4 ratio of medium and to Matrigel. This material is then transferred to a print cartridge, incubated at 17°C for 30 minutes, and bioprinted into each well at a pressure between 12 and 15 kPa (**Figure 1B**).

Using this protocol, standard prints on glass-bottom plates have a thickness of approximately 200 µm (**Figure 1B**). The HSLCI platform uses a wavefront sensing camera and a dynamic focus stabilization system to perform continuous, high-throughput quantitative phase imaging of biological samples, tracking their biomass changes over time[23,24]. When an object of interest is out of focus, phase information obtained with the interferometric camera cannot be assumed to

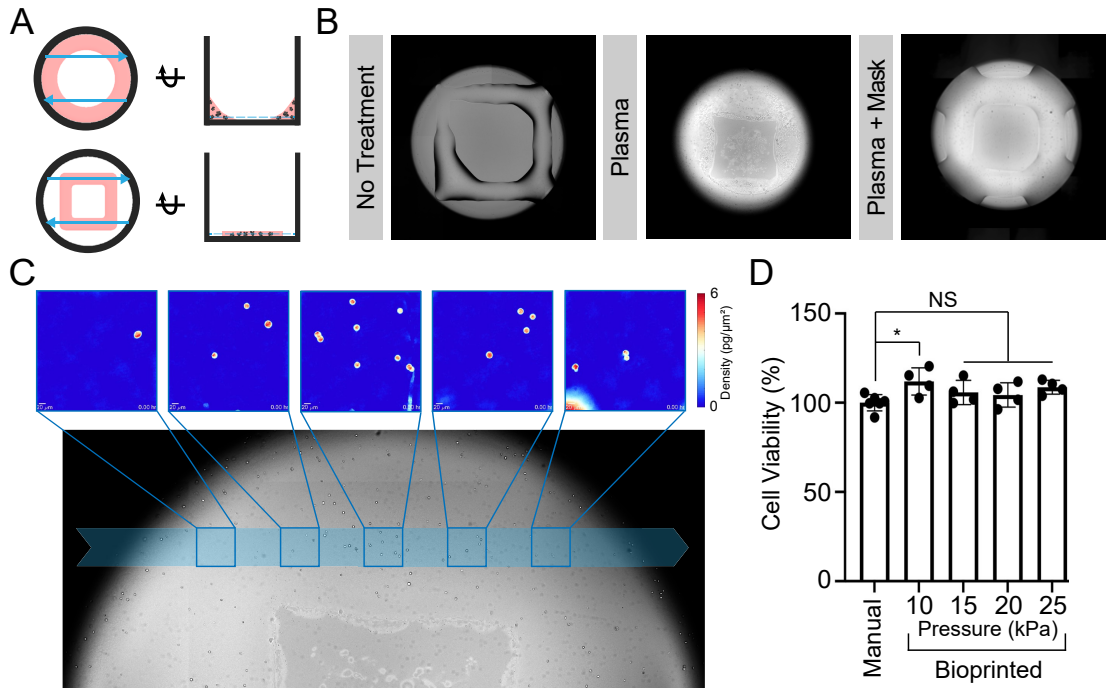

Figure 1. Bioprinting thin layers of cells for HSLCI. (A) Schematic of wells with mini-rings (top) and mini-squares (bottom) relative to HSLCI imaging path (blue arrows). The top views (left) demonstrate that transitioning from rings to squares increases the amount of material in the imaging path of the interferometer. The side views (right) show that organoids in the square geometry align to a single focal plane better than organoids in a ring. **(B)** Plasma treatment of the well plate prior to printing optimizes hydrogel construct geometry. Bioprinting Matrigel onto untreated glass (left) generates thick (~200µm) constructs. Whole well plasma treatment (middle) increases the hydrophilicity of all well surfaces causing the Matrigel to spread thin (~50µm) over the surface. Plasma treatment with a well mask facilitates the selective treatment of a desired region of the well (right) for constructs with a uniform thickness of approximately 75 µm. **(C)** Individual organoids can be tracked over time across imaging modalities. Five representative HSLCI images are traced to the imaging path across a brightfield image. **(D)** Cell viability of printed versus manually seeded MCF-7 cells in a Matrigel-based bioink. An ordinary one-way ANOVA was performed ($p = 0.0605$) with post-hoc Bonferroni's multiple comparisons test used to compare all bioprinted conditions against the manually seeded control.

maintain its direct relationship with the sample's dry biomass[26]. Thus, by generating thin layers of Matrigel, we can have a large number of organoids in focus that can be quantitatively assessed at any given time. To generate thinner (<100 μm) constructs amenable to efficient HSLCI imaging, we increased the hydrophilicity of the glass surface by oxygen plasma treatment[47]. We developed 3D masks composed of BioMed Amber Resin (FormLabs) to selectively functionalize the region of interest (**Figure S1**, see Materials and Methods). Bioprinting post-plasma treatment generated uniform mini-squares with organoids closely aligned on a single focal plane at (~70 μm) thickness (**Figure 1B**). We therefore proceeded to verify that thin, printed mini-squares are amenable to massively parallel QPI by HSLCI (**Figure 1C**). Bioprinted organoids can be easily imaged by aligning the legs of the printed mini-square constructs with the HSLCI imaging path (**Figure 1C**).

Lastly, we verified if the printing parameters used altered cell viability by directly comparing MCF-7 cells manually seeded according[3,15,16] to cells printed through a 25G needle (260 μm inner diameter) using extrusion pressures ranging from 10 to 25 kPa. We did not observe any reduction in cell viability as measured by ATP release assay (**Figure 1D**). These results are consistent with the existing literature as reductions in cell viability are often associated with higher print pressures (50-300 kPa) which are oftentimes used for extruding more viscous materials[48,49]. Overall, we have optimized a protocol that generates bioprinted layers suitable for high-throughput HSLCI imaging without impacting cell viability. By having a cell-free well center, the mini-squares retain automation compatibility that is crucial for robust downstream applications[3,15,16,50,51].

Bioprinted tumor organoids maintain histological features of manually seeded organoids. Next, we directly compared the histology and immunohistochemical profiles of bioprinted and hand-seeded or-

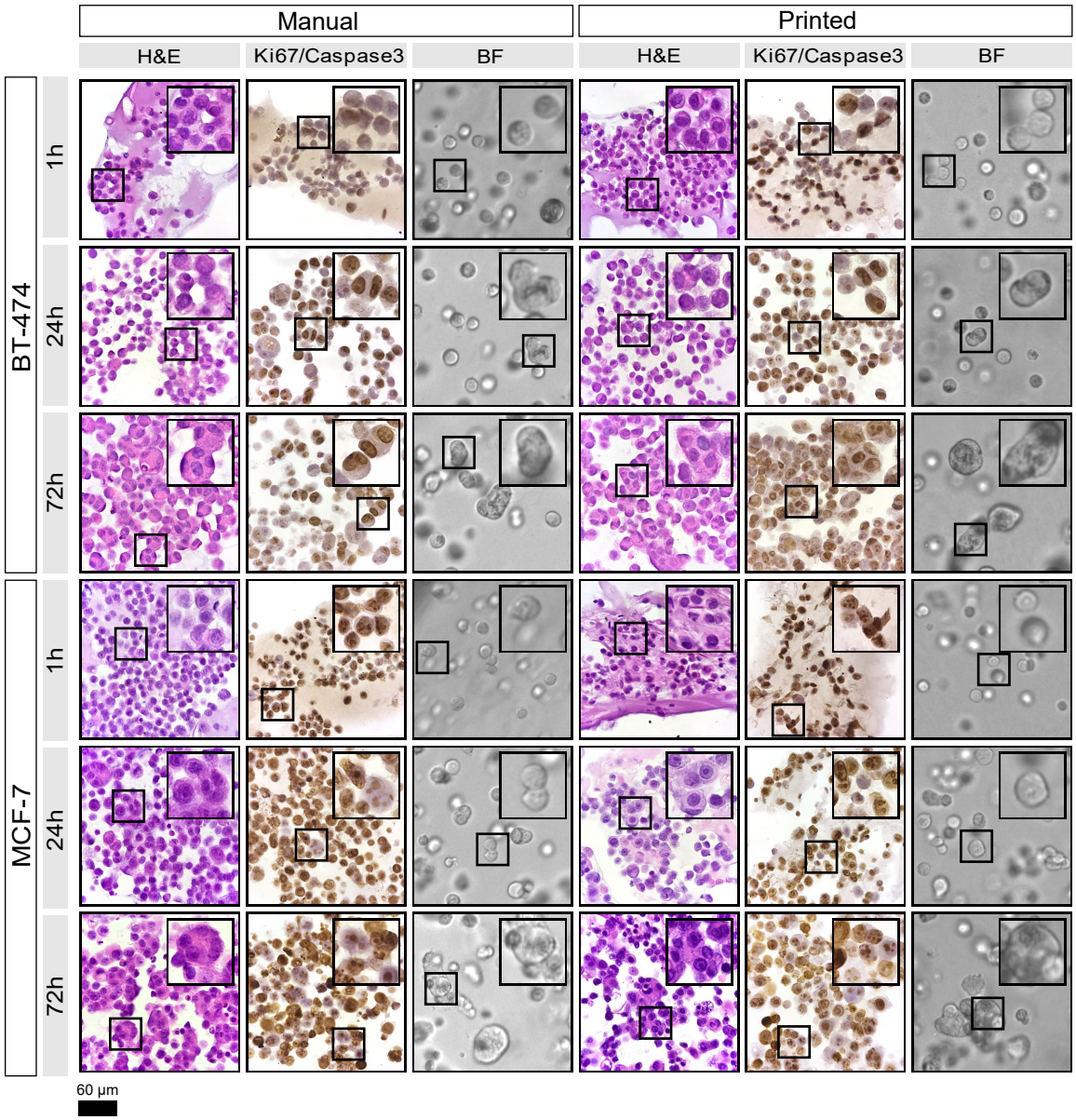

Figure 2. Bioprinted cells and organoids retain the histopathology of their manually seeded counterparts. H&E staining shows the development of multicellular organoids over time regardless of seeding method. The prevalence and size of multinuclear organoids increase with culture time. Ki-67/Caspase-3 staining demonstrates that most cells remain in a proliferative state throughout culture time. While apoptotic cells were observed in organoids cultured for 72 hours, the majority of cells show strong Ki-67 positivity. All images are 40X magnification and insets are 80X magnification. Ki-67 is shown brown, and caspase-3 in pink.

ganoids generated from two breast cancer cell lines, BT-474 and MCF-7, with different molecular features and human epidermal growth factor receptor 2 (HER2) and estrogen receptor (ER) status[52]. We seeded cells as maxi-rings (100,000 cells/ring) to retain sufficient material for downstream characterization. Cells were either manually seeded into 24 well plates[3,15,16] or in 8-well plates at an extrusion pressure of 15 kPa. The bioprinted cells and resulting organoid structures are morphologically indistinguishable from the manually seeded counterparts as visible in brightfield images and H&E-stained sections taken 1, 24 and 72 hours after seeding (**Figure 2**). Both bioprinted and manually seeded samples grew in size over time. Bioprinting did not alter proliferation (Ki-67 staining) or apoptosis (cleaved caspase-3; **Figure 2**). Hormone receptor status was unaltered as shown by IHC for HER2 (**Figure S2**) and ER (**Figure S3**). These results are in agreement with literature reports of receptor status for both cell lines[53–56]. Overall, bioprinting did not influence histologic features.

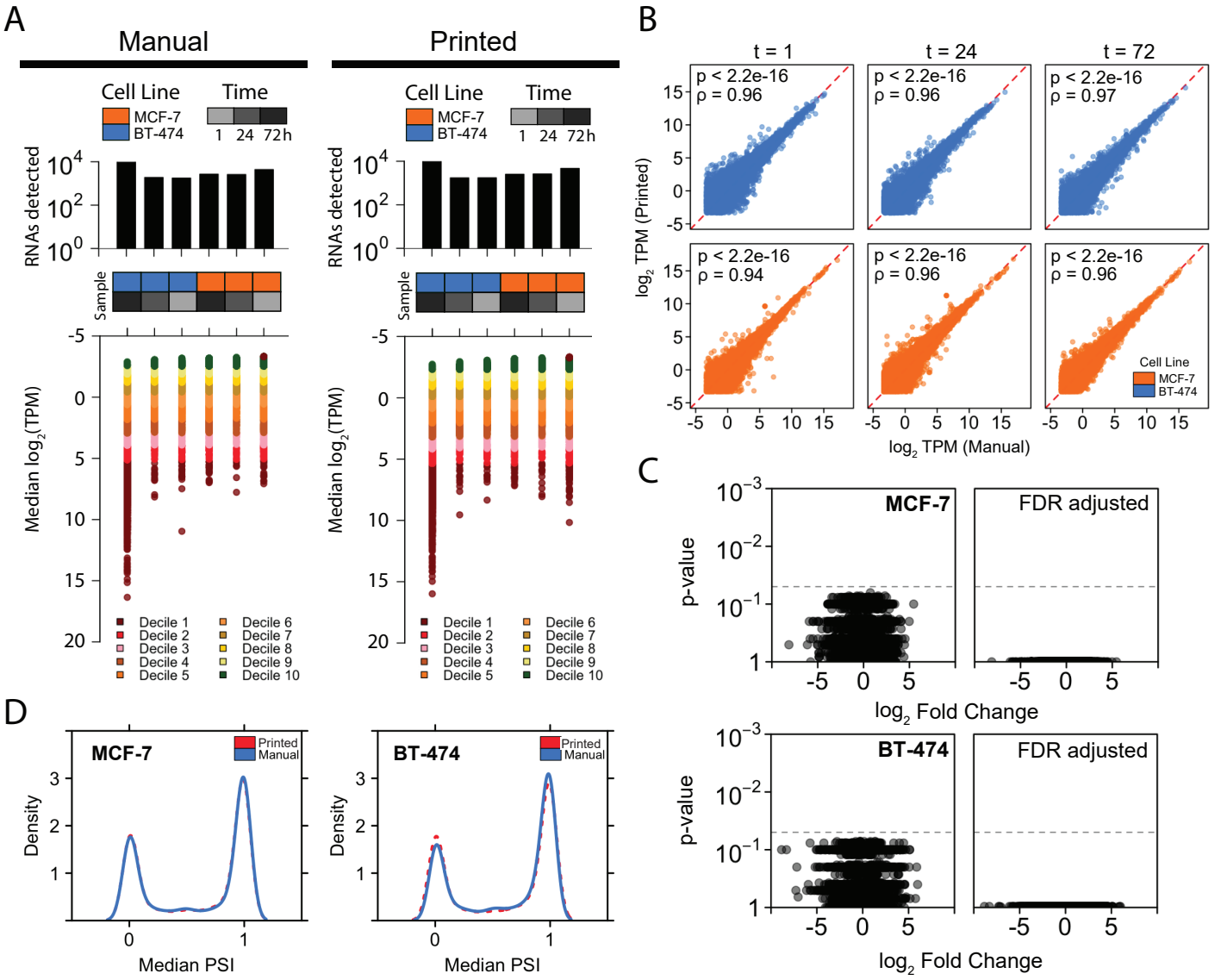

Figure 3. Bioprinting does not alter the transcriptome of cells and organoids. **(A)** Distributions of total number of transcripts detected (above) and transcript abundances (below) measured as transcripts per million (TPM) organized into groups of deciles based on median abundance. **(B)** RNA abundances ($\log_2$ TPM) of manually seeded and bioprinted organoids at three different time points (t = 1, 24, and 72 hours). Spearman's ρ was assessed for each association. We found strong associations between RNA abundances derived from printed and manually seeded organoids for both cell lines. **(C)** Volcano plots of Mann-Whitney U-test results for MCF7 and BT474 organoids with unadjusted p-values (left) and false discovery rate (FDR) adjusted p-values (right) comparing the RNA abundances of transcripts between manually seeded and printed tumor organoids. Fold change of RNA transcripts were assessed and $\log_2$ transformed. No transcripts were preferentially expressed based upon seeding method for organoids of either cell line (n = 0 out of 27,077 genes, q-value <0.1, Mann-Whitney U-test). **(D)** Median percent spliced in (PSI) of exon skipping isoforms were similarly distributed among MCF7 (left) and BT474 (right) derived organoids. Distribution of isoforms is consistent between manually seeded (blue) and bioprinted (red) organoids. PSI of 1 indicates that the isoform is exclusively an exon inclusion isoform, while a PSI of 0 indicates that the isoform is exclusively an exon skipping isoform.

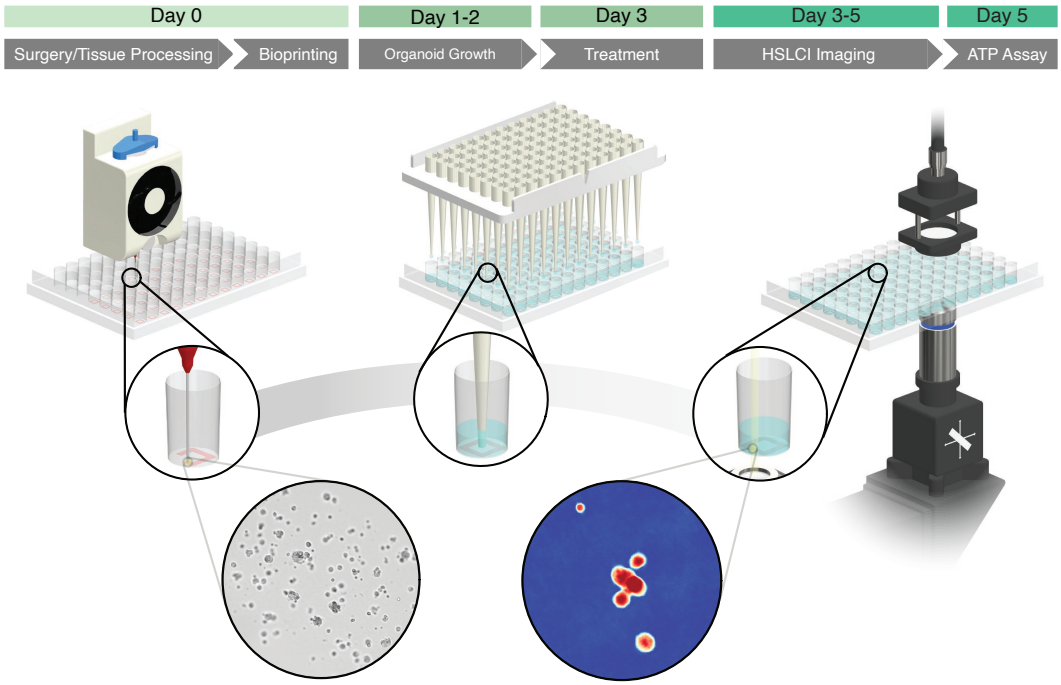

Figure 4. Bioprinted organoids HSLCI screening pipeline. Extrusion-based bioprinting is used to deposit single-layer Matrigel constructs into a 96-well plate. Organoid growth can be monitored through brightfield imaging. After treatment, the well plate is transferred to the high-speed live cell interferometer for phase imaging. Coherent light illuminates the bioprinted construct and a phase image is obtained. Organoids are tracked up to three days using the interferometer and changes in organoid mass are measured to observe response to treatment.

Bioprinted and manually seeded organoids are molecularly indistinguishable. To further support our findings that the bioprinting protocol we implemented has minimal impacts on the organoids, we also analyzed the transcriptome of manually seeded and bioprinted cells 1, 24 and 72 hours post-seeding. We assessed the distributions of 27,077 RNAs and clustered these into deciles based on their median abundance and found no significant difference in distribution between cell seeding approaches (**Figure 3A**). The overall transcriptomes of manually seeded and bioprinted organoids were extremely well-correlated (**Figure 3B**). Similarly, no individual transcripts differed significantly in RNA abundance in either cell line (0/27,077 genes, q <0.1, Mann-Whitney U-test; **Figure 3C**).

Transcript abundances can be unchanged, but variations in pre-mRNA alternative splicing events can induce functional changes[57–59]. We found that the density of exon-inclusion and exon-skipping isoforms was unchanged, with no individual fusion isoforms associated with the organoid printing method in either cell line (0/8,561, q <0.1, Mann-Whitney U-test; **Figure 3E**). Similarly, the number of fusion transcripts were not associated with seeding method (p = 0.17, Mann-Whitney U-test), although with large numbers of singletons detected in only a small number of samples (**Figure S4A**). Finally, we considered RNA editing; again, we found no significant differences in the number of RNA editing sites between printed and manually developed tumor organoids (p = 0.48, Mann-Whitney U-test; **Figure S4B**). These findings demonstrate that our bioprinting protocol does not significantly impact RNA expression, splicing, fusions, or editing sites on short or longer timescales, preserving their molecular profiles while introducing favorable features like reduced thickness suitable for high-throughput imaging using HSLCI.

Trends in mass accumulation of bioprinted organoids can be quantified by HSLCI with single organoid resolution. The full organoid screening pipeline includes cell bioprinting (day 0), organoid establishment (day 0-2), full media replacement (day 3, **Figure 4**) followed by transfer to the HSLCI incubator. Within 6 hours of media exchange, the plates are continuously imaged for the following 48-72 hours. At the end of the imaging period, we perform an endpoint ATP assay to assess cell viability (**Figure 4**).

Using HSLCI-based imaging allowed real-time tracking of n=67 MCF-7 organoids in n=8 interpretable replicate wells (8.38/well) and n=101 BT-474 organoids in n=12 interpretable wells (8.42/well) 6 hours after treatment (**Figure 5A**). After 48 hours, the number of tracked organoids increased marginally for both MCF-7 (n=89 organoids; n=8 wells; 11.13/well) and BT-474 organoids (n=106 organoids; n=10 wells; 10.6/well) (**Figure 5A**). Over the entire imaging period, n=219 MCF-7 and n=265 BT-474 organoids were tracked for at least six hours. The number of organoids tracked can be improved by using position-specific reference images during pre-processing, analyzing more fields of view within each well, and implementing different image segmentation and tracking algorithms.

Next, we determined the mass of each organ-

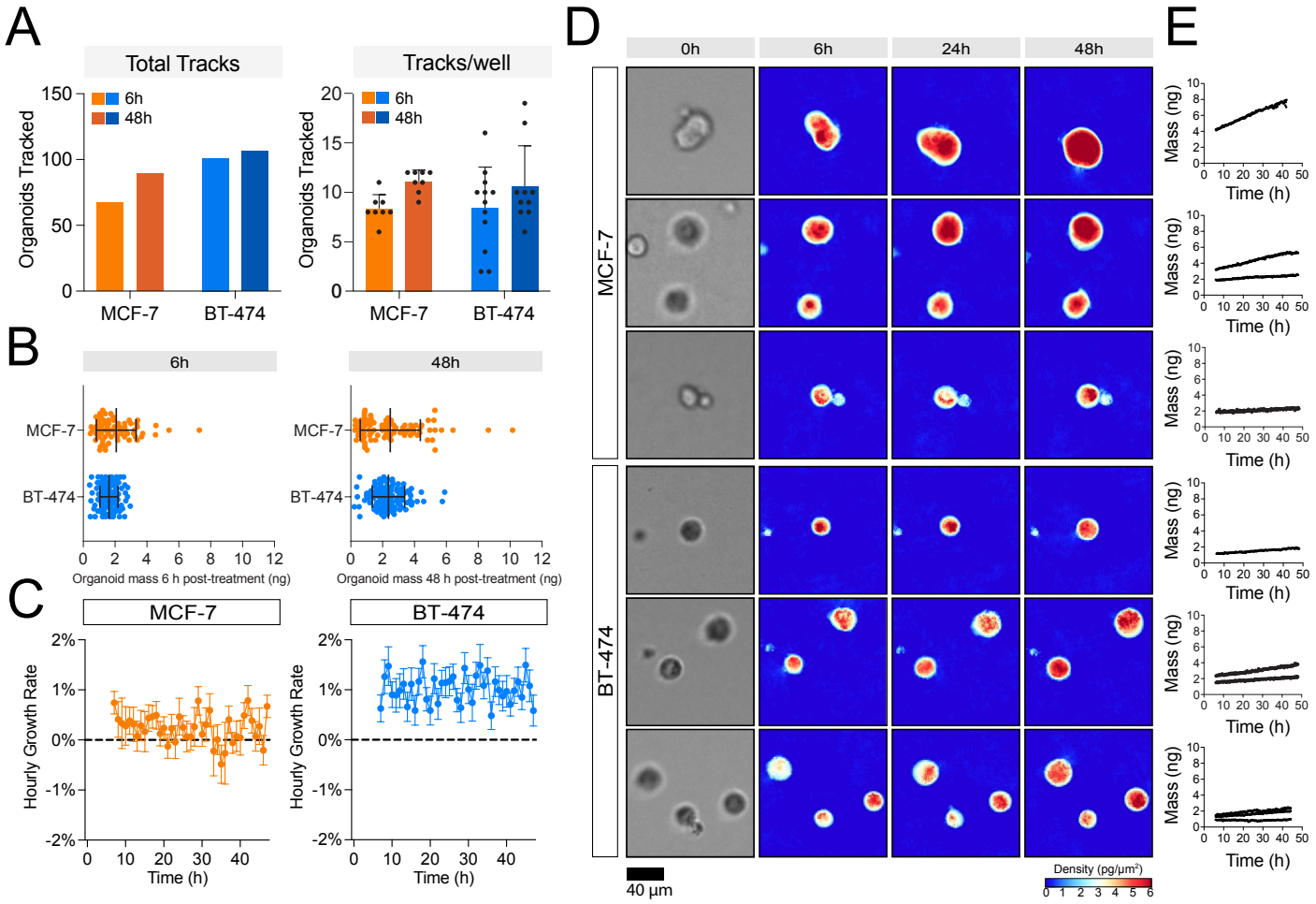

Figure 5. Bioprinted organoids can be tracked by HSLCI. (A) Total number of organoid tracks (left) and mean number of tracks per well (right) 6 hours (pale) and 48 hours (dark) after treatment for each cell line. The total number of organoid tracks across interpretable, replicate wells was 67 for MCF-7 organoids (n = 8), and 101 for BT-474 organoids (n = 12). At the 48-hour time-point the total number of tracks was 89 and 106 for MCF-7 (n = 8) and BT-474 (n = 10), respectively. **(B)** Mass distribution of tracked organoids 6h and 48h after treatment. Black bars represent the mean with error bars representing the standard deviation. **(C)** Hourly growth rate (percent mass change) of tracked MCF-7 (left) and BT-474 (right) organoids cultured in 1% DMSO. **(D)** Representative images of MCF-7 and BT-474 organoids tracked with HSLCI. Brightfield images of organoids taken immediately before treatment are shown on the left. **(E)** Calculated mass of each representative organoid over time.

oid by converting interferograms to phase shift images using the SID4 software development kit[26]. Organoid mass was calculated by integrating the phase shift over the organoid area and multiplying by the experimentally determined specific refractive increment[25,42–45]. At the beginning of the imaging period, the average organoid mass was slightly larger for MCF-7 (2.0 ± 1.2 ng) than BT-474 organoids (1.6 ± 0.5 ng, **Figure 5B**). The difference persisted after 48 hours with MCF-7 organoids averaging 2.5 ± 1.9 ng and BT-474 organoids growing to 2.4 ± 1.0 ng. BT-474 cells grew at a rate of 1.01 ± 3.13% per hour while MCF-7 organoids demonstrated slower average hourly growth rates (0.23 ± 2.92% per hour, **Figure 5C**). The growth rate of the 3D BT-474 organoids is comparable to that observed after 6 hours in 2D culture (approximately 1.3%), while the MCF-7 organoids showed a lower growth rate than previously reported 2D cultures (approximately 1.7%)[29]. We also observed a positive association between initial organoid mass and growth rate (95% confidence interval of slope is 0.1040 to 0.2993), but only for MCF-7 organoids (**Figure S5**).

While the average parameters quantified above offer a population-wide picture of organoid behavior, the power of HSLCI imaging is its ability to quantify intra-sample heterogeneity. We identified several mechanisms by which organoids gained mass over time, including cell growth, cell division, and/or the aggregation of multiple cells or small organoids (**Figure 5D-E, Supplementary Videos 1 & 2**). We quantified the ratio of organoids that gained, lost, and maintained mass over 12, 24, and 48 hours (**Figure S6, Table S1**). In the absence of drug treatment, 1.9% of BT-474 organoids lost more than 10% of their initial mass and 82.1% gained more than 10% of their initial mass over

48 hours. In contrast, only 37.1% of MCF-7 organoids gained mass and 20.2% lost mass. The heterogeneity in the organoid populations also becomes evident over time as 20.4% of MCF-7 organoids gained more than 10% mass within 12 hours. This proportion nearly doubles to 36.7% after 24 hours but remains consistent with a marginal increase to 37.1% after 48 hours. This pattern differs from BT-474 organoids as the population of organoids that gained mass continually increases over 48 hours. The proportion of organoids that gained >10% mass increases from 31.2% after 12 hours, to 61.8% after 24 hours, and 82.1% after 48 hours. Overall, our data confirms that HSLCI can be used to image tumor organoids in 3D, and to quantify both population- and single organoid-level characteristics and heterogeneity.

Time-dependent differences in drug response of organoids can by quantified by HSCLI. We then tested the utility of our platform in detecting drug responses in high-throughput 3D screenings (**Figure 4**). As proof-of-principle we tested staurosporine, a non-selective protein kinase inhibitor with broad cytotoxicity[60], and lapatinib, a targeted small molecule tyrosine kinase inhibitor targeting EGFR and HER2[61]. Drugs were tested at concentrations between 0.1 and 50 μM. This range includes and extends beyond the maximum plasma concentration reported for lapatinib (4.2 μM)[62].

Representative HSLCI images demonstrate a range of responses to treatment (**Figure 6A**). The average masses at 6 hours post-treatment are not significantly different from the vehicle control (**Figure 6B**, **Table S2**). After 48 hours, we observed significant differences in a number of treated samples (**Table S2**). Control MCF-7 organoids averaged 2.48 ± 1.89 ng, while those treated with 1 μM and 10 μM staurosporine showed significant reductions in average masses to 1.33 ± 1.08 ng ($p = 0.0121$, Dunnett's multiple comparisons test) and 1.26 ± 0.80 ng ($p = 0.0086$, Dunnett's multiple comparisons test), respectively.

BT-474 organoids showed a similar pattern with control organoids averaging 2.36 ± 1.02 ng and staurosporine-treated organoids averaging 0.70 ± 0.26 ng (1 μM, $p < 0.0001$, Dunnett's multiple comparisons test) and 0.83 ± 0.72 ng (10 μM, $p < 0.0001$, Dunnett's multiple comparisons test). The normalized growth curves rapidly show response to treatment with 1 μM staurosporine. After 12 hours, 33.3% of the tracked BT-474 organoids lost mass compared to 3.2% in the control, with a 60% reduction in the number of organoids that increased in size (31.2% vs 19%, **Figure 6C and S6, Table S1**).

Responses to lapatinib distinctly showed cell type-specific trends. MCF-7 cells exhibited a significant reduction in average mass (from 2.48 ± 1.89 ng to 1.32 ± 1.06 ng, $p = 0.0285$, Dunnett's multiple comparisons test) at 48h only when treated with 50 μM of lapatinib. Conversely, BT-474 were affected at concentrations as low as 1 μM (**Figure 6B-C and S6, Table S2**). Our analysis shows that 4.3% of all MCF-7 organoids continue to grow in the presence of 50 μM of lapatinib and an additional 43.5% maintained their mass after 48 hours of treatment (**Figure 6C, Figure S6, Table S1**). BT-474 organoids show a dose-dependent response when treated with lapatinib, with concentrations of 0.1, 1, 10 and 50 μM leading to 6.5%, 22.5%, 37.7%, and 84.6% of all BT-474 organoids losing mass (vs 1.9% for controls, **Figure 6C**). The heightened sensitivity of BT-474 cells to lapatinib is expected given the higher expression of HER2 found in these cells[52] (**Figure S2**).

We consistently observed a fraction of organoids that do not respond to treatment across all conditions (**Figure 6C, Figure S6, Table S1**). For instance, a fraction of the MCF-7 organoids treated with 50 μM lapatinib on average grew at similar rates as vehicle-treated cells after 36 h of treatment (**Figure 6D**). While overall more sensitive to lapatinib (**Figure 6**), we could also pinpoint individual BT-474 organoids that did not respond (white arrow, **Figure 6A**). Our findings are indicative of a resistant population of organoids that can be rapidly identified by HSLCI imaging.

To validate the responses measured by HSLCI, we performed an endpoint ATP-release assay on the same plates used for HSLCI imaging to assess organoid viability after 72h of treatment (**Figure 6E**). The ATP assay confirmed that both cell lines are highly sensitive to staurosporine treatment with near-zero viability when treated with 1 and 10 μM concentrations. Additionally, BT-474 organoids show significant reductions in viability when treated with 0.1 μM lapatinib for 72 hours (**Table S3**). Overall, the results of the cell viability assay after 72 hours confirm the trends observed in as little as 12 hours by HSLCI.

Discussion

Cancer therapy is increasingly moving towards treatments tailored to each patient's unique and heterogeneous disease[63,64]. Molecular precision medicine requires knowledge of the associations between molecular features and drug response[1,65]; however, in most instances these relationships have yet to be established[66]. Functional precision medicine bypasses the need to have prior knowledge of these associations while simultaneously generating data to identify them. The key limitations towards the broad adoption of

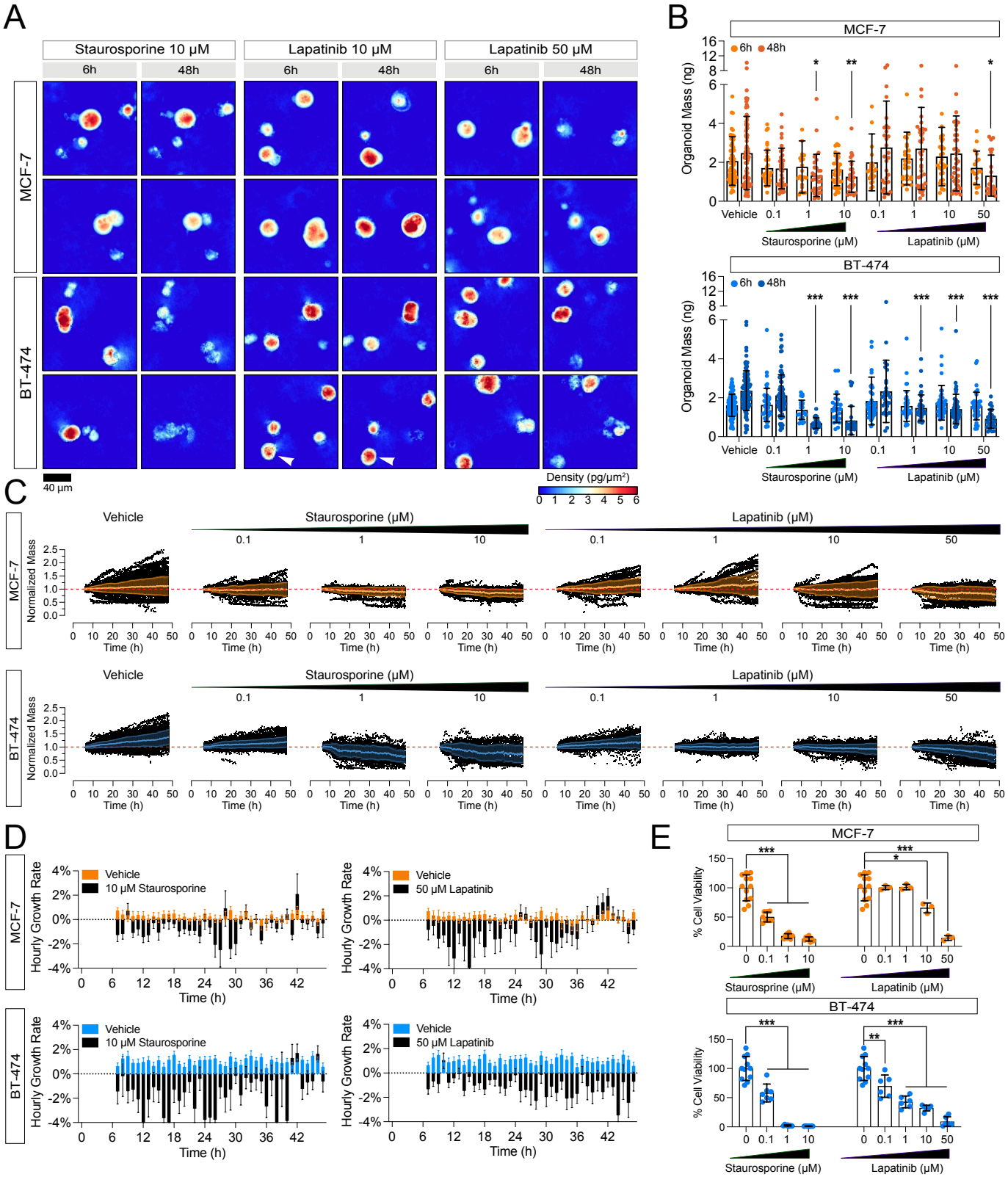

Figure 6. HSLCI enables high-throughput, longitudinal drug response profiling of 3D organoid models of cancer. (A) Representative images of organoids treated with 10 μM staurosporine, 10μM lapatinib, and 50μM lapatinib. The white arrow annotates a BT-474 organoid that gains mass when treated with 10 μM lapatinib. **(B)** Mass of tracked MCF-7 and BT-474 organoids by treatment. The left bars and pale points represent organoid mass after 6 hours of treatment and the right bars and dark points represent organoid mass after 48 hours of treatment. **(C)** Scatterplots of normalized organoid pass over time. All organoid tracks for each treatment condition are shown on each plot. The mean normalized mass ± standard deviation is also shown in orange (MCF-7) and blue (BT-474). **(D)** Hourly growth rate comparisons (percent mass change) between organoids treated with 10μM staurosporine and vehicle, and 50μM lapatinib and vehicle. **(E)** Percent cell viability of treated wells determined by an ATP-release assay. $p<0.05$ is denoted by *, $p<0.01$ is denoted by **, and $p<0.001$ is denoted by ***.

functional precision medicine have been the creation of physiological organoid culture models, the development of high-throughput systems, and the difficulty in measuring organoid heterogeneity. Our pipeline surmounts each of these barriers by incorporating an array of robust 3D organoid cultures in a standardized well plate format that facilitates single-organoid analysis of response to treatment.

The broad adoption of functional precision medicine requires scalable, easy to analyze, physiologically relevant tumor models. We introduced bioprinting to enhance the throughput and consistency of our previously published organoid models[3,15,16]. We opted to print a Matrigel-based bioink due to its ability to preserve tumor characteristics in vitro[3]; however, its weak mechanical integrity and its temperature-dependent viscosity and crosslinking behavior limit its suitability for bioprinting[67]. To circumvent these limitations, we found that incubating the material at 17°C for 30 minutes yielded the most consistent mechanical properties for bioprinting (**Figure 2**). Our findings align with the existing consensus that consistent bioprinting with Matrigel is difficult to achieve, but simple, single-layer structures are attainable with strict temperature regulation. We further enhanced the quality of the Matrigel deposition by selectively modifying the print substrate with oxygen plasma. The introduction of 3D plasma masks (**Figure S1**) facilitated the selective treatment of a square region in each well. The increased hydrophilicity of the substrate in the exposed region guides the spreading of the material to ensure maximize consistency in deposition volume and construct thickness while preventing obstruction of the center of the well. Bioprinting allowed us to finely control the size and shape of the deposited gel constructs, facilitating the use of HSLCI for downstream analysis.

To our knowledge, this is the first reported use of live cell interferometry for time-resolved quantitative analysis of 3D organoid cultures. Previous studies have used interferometry to quantify the mass of individuals cells cultured on 2D substrates to study cell division[68], cytoskeletal remodeling[69], mechanical properties[70], and response to treatment[23–25]. Tomographic QPI has also been used to obtain high-resolution images of 3D objects such as cerebral organoids[71]. The primary challenge of adapting live cell interferometry for the mass quantitation of 3D organoids is maintaining the organoids in a single focal plane. The mass of organoids outside of the focal plane cannot be accurately calculated as phase information for out-of-focus planes is difficult to interpret[26]. We were able to circumvent this challenge by introducing bioprinting to generate uniform, thin constructs to maximize the number of organoids that could be tracked in parallel. Despite these efforts, the efficiency of imaging is relatively limited thus far with only approximately 20 (approximately 1%) organoids analyzed per well. These datasets are limited by the 6-hour delay between drug treatment and imaging, and it is possible that highly sensitive organoids undergo cell death prior to the start of tracking. The use of region-specific reference images in the unwrapping process may also increase the number of quantifiable organoids. Finally, we plan to further optimize our image segmentation and organoid tracking algorithms to increase the number and continuity of organoid tracks.

Despite the development of 3D cancer models with varying extents of complexity and scalability, functional screening assays have been hindered by their inability to consider the heterogeneity of tumor response. Genomic characterization of tumors has demonstrated that these malignancies are collections of evolutionarily-related subclones, rather than homogeneous[72–75]. This genetic diversity is one of the several factors that contributes to differential response to treatment. Endpoint assays, such as live-dead staining or ATP-release quantification, characterize the average response to treatment. Though they may be useful for identifying drug sensitivity in majority cell populations, they fail to account for the response of resistant populations that may also be present. In the clinical setting, failure to treat the resistant populations may lead to initial response, followed by recurrence and long-term disease progression[76–78]. The power of HSLCI is its ability to non-invasively track various features of the organoids over time, including size, motility, and mass density. Because of the ability to quantitatively measure mass changes in response to treatment, it is possible to identify and isolate responsive, agnostic, and resistant subpopulations of cells which can lead to more informed clinical decision making when selecting the treatment approach[28].

Acknowledgments

We would like to acknowledge the UCLA Translational Pathology Core Laboratory and the UCLA Technology Center for Genomics and Bioinformatics for their assistance with this work. Additionally, we would like to thank Dr. Steven Jonas for his generous access to laboratory equipment. This work was supported by a NIH R01CA244729 (to A.S.), a National Science Foundation Graduate Research Fellowship (DGE-2034835, to B.W.), a Eugene V. Cota Robles Fellowship (to B.W.) a UCLA DGSOM Seed Award (to A.S. and P.C.B.), the Air Force Office of Scientific Research (FA9550-15-1-0406, to M.A.T.), the Department of Defense (W81XWH2110139, to M.A.T.). It was addition-

ally supported by NIH U24CA248265 (to P.C.B.) and NIH R01GM114188, R01GM073981, R01CA185189, R21CA227480, R01GM127985, and P30CA016042 (to M.A.T.). A.S., P.J.T., B.W. and N.T. are inventors on a patent application based on some aspects of this work.

Materials and Methods

2D Cell Culture

MCF-7 and BT-474 breast adenocarcinoma cell lines were obtained from the American Type Culture Collection (ATCC). All cell lines were grown for a maximum of 10 passages in RPMI 1640 (Gibco 22400-089) supplemented with 10% fetal bovine serum (FBS, Gibco 16140-071) and 1% antibiotic-antimycotic (Gibco 15240-062). Both cell lines were authenticated by short tandem repeat profiling using the GenePrint 10 kit (Laragen).

Manually Seeding 3D Organoids

Organoids were seeded manually according to our previously published protocols[3,15,16]. Briefly, single cells suspended in a 3:4 mixture of Mammocult (StemCell Technologies 05620) and Matrigel (Corning 354234) were deposited around the perimeter of the wells of either 24-well or 96-well plates. The cell suspension was kept on ice throughout the seeding process to prevent gelation of the Matrigel. To seed organoids in a 96-well plate (Corning 3603), a pipette was used to distribute 5μL of cell suspension (5×105 cells/mL) along the bottom perimeter of each well; this “mini-ring” seeding geometry facilitated automatic changes of media and addition of drugs with a liquid handling system. Every eight wells, the cell suspension was briefly vortexed, and the pipette tip was exchanged. Once all mini-rings are generated, plates were incubated at 37°C and 5% CO2 for 20 minutes to solidify the Matrigel, and 100μL of pre-warmed Mammocult was added to the center of each well using an epMotion 96 liquid handler (Eppendorf). To generate larger rings (maxi-rings) in 24-well plates (Corning 3527), 70μL of cell suspension (1.4×106 cells/mL) was deposited around the perimeter of each well. After every three wells, the cell suspension was vortexed, and the pipette tip was replaced. Following seeding, the plate was incubated at 37°C and 5% CO2 for 45 minutes to solidify the Matrigel, and 1mL of pre-warmed Mammocult was added to the center of each well.

3D Printing Plasma Masks

Custom well masks were designed to meet the specifications of the well plates that were used in these experiments. The design was generated in Inventor 2020 (Autodesk) and printed using a Form3B (FormLabs). We elected to use the Biomed Amber resin (FormLabs) to generate these constructs due to its biocompatibility and ability to be autoclaved. The design was exported as an STL file and imported into the PreForm (FormLabs) software to arrange the parts. After printing, parts were post-processed in two washes of isopropanol, air-dried for at least 30 minutes, and cured for an additional 30 minutes at 70°C in the Form Cure (FormLabs).

Bioprinting 3D Organoids

Cells were bioprinted using a CELLINK BioX with a Temperature-Controlled Printhead. Gcode files were written to print the desired single-layer geometry. We wrote standardized blocks of Gcode encode the print path for the repeated geometries. MATLAB (MathWorks, Inc.) was used to integrate these standardized blocks into full Gcode files with the defined coordinates for each well. We used 8-well plates when printing the larger constructs as the depth of the well in a standard 24-well plate prohibited the use of 0.5” length needles. Large rings were necessary to deposit a sufficient number of cells for RNA-Seq and IHC. Four rings with a diameter of 14.5mm were printed for RNA sequencing (approximately 200,000 cells total), while four sets of concentric 14.5mm, 12.5mm, and 10.5mm diameter rings were used for IHC analysis (approximately 500,000 cells total). We printed mini-squares with side length 3.9mm for drug screening and HSLCI imaging. The mini-squares were inscribed within the circular well with sides parallel to the sides of the well plate. The open center of the constructs facilitates automatic manipulation with fluid handling equipment while the sides of the square are positioned to maximize the number of organoids imaged by HSLCI. The bioprinting process utilized the same material deposited for manually seeded organoids. A single cell suspension in a 3:4 mixture of Mammocult and Matrigel was prepared on ice. After vortexing briefly to homogenize, the mixture was transferred into a 3mL syringe by removing the plunger and capping the opposite end. Once the plunger was replaced, the syringe was inverted, and bubbles were forced out of the tip. The material was then transferred to a room temperature 3mL bioprinter cartridge (CELLINK) by connecting the syringe and cartridge with a double-sided female Luer lock adapter (CELLINK). Any air bubbles in the syringe were removed and the loaded cartridge was incubated in a rotating incubator (Enviro-Genie, Scientific Industries) for 30 minutes at the print temperature.

During the incubation period, the printer was sterilized

with the built-in UV irradiation function and the printhead was set to the print temperature. During this time, we treated the 96-well plates with oxygen plasma to improve the hydrophilicity of the surface. The well masks were autoclaved prior to use. The masks were inserted into the well plate and pressed in contact with the glass surface. Rubber bands were used to hold the masks in place and ensure conformal contact was maintained throughout the plasma treatment. The well plates were treated with oxygen plasma in a PE-25 (Plasma Etch) for 30-90 seconds, 15 minutes prior to bioprinting. After plasma treatment, the well plate was placed in the bioprinter and Automatic Bed Levelling (ABL) was performed.

Once the incubation period ended, we attached a 0.5" 25-gauge needle and loaded the cartridge into the precooled printhead. We primed the needle by extruding a small volume of material at 15kPa prior to calibrating the printer. Just before printing, we cleared the needle of the gelled material by extruding a small volume using 40 kPa prior to starting the print. To create constructs of the appropriate thicknesses, prints in 8-well plates were extruded at 15k Pa while prints in 96-well plates were extruded at 12-15 kPa. The bioprinter completes the deposition process for 96-well plates in approximately four minutes. After printing, the constructs were incubated at 37°C for at least 30 minutes to solidify the matrix and 100μL of Mammocult medium was then added.

Assessment of Viability After Bioprinting

The viability of manually seeded and bioprinted organoids was compared using an ATP assay. Manually seeded organoids were prepared in accordance with the protocol described above and published3,15,16. To assess the viability of bioprinted organoids, we prepared the bioink and bioprinter as described. Instead of printing the bioink into a well plate, we extruded 100 μL of bioink into and Eppendorf tube for each print pressure (10, 15, 20, and 25 kPa). We seeded four 10μL rings in a 96-well plate using the extruded bioink. We then added 50 μL of 5 mg/mL Dispase (Life Technologies 17105-041) solution to each well and incubated for 25 minutes. After shaking for 5 minutes on an orbital shaker at 80 RPM, we added 75μL of CellTiter-Glo® Luminescent Cell Viability Reagent (Promega G968B) to each well and followed the manufacturer's instructions. Luminescent readings were taken on a SpectraMax iD3 (Molecular Devices) plate reader. The viability of each well was calculated by normalizing the luminescent signal to the average signal from the manually seeded control wells. An ordinary one-way ANOVA with post-hoc Bonferroni's multiple comparisons test was performed in GraphPad Prism.

Immunohistochemistry

Immunohistochemical staining was performed on manually seeded and bioprinted organoids seeded in 24 or 8-well plates, respectively. A detailed procedure has been published independently[15]. The samples were prepared for histological analysis by carefully aspirating all media from the well without disrupting the construct and washing with pre-warmed PBS. The PBS was added dropwise to the center of the well to avoid delamination and fragmentation. After aspirating all remaining liquid from the well, we added 10% buffered formalin (VWR 89370-094) and followed by incubating at 37°C. After the 5-minute incubation, the plates were transferred to ice for 30 minutes before storage in a 4°C refrigerator until collection. The fixed organoids were harvested within 3 days using a pipette tip to scrape the surface of the wells, the organoids were subsequently transferred to a conical tube. The organoids were pelleted by centrifugation at 2000xg for 5 minutes and the supernatant was aspirated; this process was repeated twice to remove as much liquid as possible. HistoGel (Thermo Scientific HG-40000-012) was then added to the pellet. Cells were mixed with the HistoGel by briefly vortexing before placing on ice to solidify. Cassettes were labeled and 5μL of HistoGel was used to coat a region of the bottom surface. Once solidified, the cell pellet in HistoGel was placed in the cassette and an additional 4μL of HistoGel was added to the top of the pellet for stability. We wrapped cassettes in parafilm and chilled them on ice for 3 minutes before unwrapping and immersing in 70% ethanol. The cassettes were then sent to the UCLA Translational Pathology Core Laboratory (TPCL) for dehydration and paraffin embedding. After embedding, 8μm thin sections were cut from the paraffin block.

Slides were baked for 20 minutes at 45 °C and de-paraffinized in xylene followed by washes in ethanol and deionized water. For H&E staining, a Hematoxylin and Eosin Stain Kit (Vector Labs H-3502) was used according to the manufacturer's protocol. For Ki-67/Caspase-3, HER2, and ER staining, Peroxidazed-1 (Biocare Medical PX968M) was applied for 5 minutes at room temperature to block endogenous peroxidases. Next, antigen retrieval was performed by immersing slides in Diva Decloaker (Biocare Medical DV2004LX) using an NxGEN Decloaking Chamber (Biocare Medical) to heat to 110 °C for 15 min. An additional 2-minute peroxidase blocking step was implemented after antigen retrieval in the Ki-67/Caspase-3 protocol. Blocking was performed at RT for 5 min with Background Punisher (Biocare Medical BP947H). Primary Ki-67/Caspase-3

staining was performed overnight with pre-diluted Ki-67/Caspase-3 (Biocare Medical PPM240DSAA) solution at 4°C, and secondary staining was performed with Mach 2 Double Stain 2 (Biocare) solution for 40 minutes at room temperature. Primary antibodies for HER2 (Novus Biologicals, CL0269) and ER (Abcam, E115) staining were diluted 1:100 in Da Vinci Green Diluent (Biocare Medical PD900L). The HER2 antibody was incubated overnight at 4°C while the ER antibody was incubated at room temperature for 30 minutes. Secondary staining was performed with Mach 3 Mouse Probe and Mach 3 Mouse HRP-Polymer for HER2 and Mach 3 Rabbit Probe and Mach 3 Rabbit HRP-Polymer for ER, all secondary staining steps were 10 minutes. Chromogen development was performed with Betazoid DAB (Biocare Medical, BDB2004) and the reaction was quenched with deionized water. Counterstaining was performed with 20% Hematoxylin (Thermo Scientific #7221) for 7.5 minutes. Slides were dehydrated in a sequence of ethanol and xylene baths before cover slips were applied with Permount (Fisher Scientific SP15-100). Imaging was performed with a Revolve microscope (Echo Laboratories). White balancing of the images was performed in Adobe Photoshop.

Sample Preparation for RNA Sequencing

Organoids were released from the Matrigel in preparation for whole transcriptome sequencing (RNA-Seq). After aspirating the media from each ring, 1 ml of cold Dispase was added per ring. After a 20-minute incubation at 37°C, the cell suspension was collected and pelleted by centrifugation at 1500xg for 5 minutes and washed with 45 ml of PBS before centrifuging again at 2000xg for an additional 5 minutes. Once all liquid was aspirated, the tubes were rapidly frozen and stored at -80°C. Frozen cell pellets (approx. 200'000 cells) were then transferred to the Technology Center for Genomics & Bioinformatics (TCGB) at UCLA for RNA sequencing. Sequencing was performed in one lane of the NovaSeq SP (Illumina) using the 2 x 150 bp paired-end protocol.

RNA Sequencing Data Processing and Analysis

FASTQ files were processed using the UCLA-CDS pipeline that includes pipeline-align-RNA v6.2.2, pipeline-quantitate-RNA v2.0.1, pipeline-quantitate-SpliceIsoform v2.0.6, pipeline-call-RNAEditingSite v5.0.0, pipeline-call-FusionTranscript v1.1.0. Pipeline-align-RNA v6.2.2 used a combination of FASTQC v0.11.9, fastp v0.20.1, STAR v2.7.6a, HISAT2 v2.2.1[31–33], Pipelinequantitate-RNA used kallisto v0.46.0, samtools v1.10, rsem 1.3.3[34,35]. Pipeline-quantitate-SpliceIsoforms used rmats v4.1.0[36]. Pipeline-call-RNAEditingSite used REDItools2 v1.0.0[37]. Pipeline-call-FusionTranscripts used STAR-Fusion v1.9.1, fusioncatcher v1.33, Arriba v2.1.0[38–40].

Samples with low transcript abundance (TPM <0.1; transcripts per million) were excluded resulting in 27,077/67,060 transcripts included in the analysis. We excluded splice isoforms with missing data in 5 or more samples (8,561 out of 17,449) due to low power. RNA editing sites were filtered to include adenosine to inosine events with sufficient coverage (q30 >10) and frequencies above 0.9. Poly-A depleted RNA included annotated microRNAs (miRNA), while poly-A enriched RNA included coding mRNAs. Raw and processed data will be made available in GEO.

We used a Mann-Whitney U-test to compare the distributions of RNA abundances, number of transcript fusions, and editing sites between bioprinted and manually seeded tumor organoids. We adjusted for multiple comparison using the false discovery rate (FDR) method. FDR values ($q < 0.1$) was the criteria for strong associations. Statistical analyses and data visualization were performed in the R statistical environment (v4.0.2) using the BPG[41] (v6.0.1) package.

High-Speed Live Cell Interferometer

HSLCI has been described previously[23,24]. The HSLCI platform is a custom-built inverted optical microscope coupled to an off-axis quadriwave lateral shearing interferometry (QWLSI) camera (SID4BIO, Phasics, Inc.)[26], motorized stages (Thorlabs) holding a single, standard-footprint (128×85 mm), glass-bottom multi-well plate, and a piezo-actuated dynamic focus stabilization system that enables continuous and repeated image collection over many fields of view (FOVs) within the sample area. All of the platform's hardware and software components are available commercially.

The HSLCI platform was installed inside a standard cell culture incubator. For all growth kinetics studies and drug screening, organoids were imaged in 96-well glass-bottom plates (Cellvis P96-1.5H-N) using a 40× objective (Nikon, NA 0.75). Organoids were seeded as single-cell suspensions in a 3:4 mixture of Mammocult and Matrigel as described above and were grown at 37 °C and 5% CO2 in Mammocult medium supplemented with 1% antibiotic-antimycotic (Gibco 15240-062). Plates were wrapped in with parafilm to limit evaporation and placed in the interferometer. The typical imaging interval was 10 minutes between successive frames at the same FOV.

Drug Screening

All drug treatments of 3D organoids were performed

in serum-free conditions in Mammocult medium supplemented with 1% antibiotic-antimycotic (Gibco 15240-062). A detailed protocol for the drug screening has been published previously[3,15]. Briefly, the culture medium was fully removed three days after seeding and replaced with 100 µL of Mammocult medium containing the indicated treatments using an automated pipetting system (EpMotion® 96). After treatment, we transferred the organoids to the HSLCI for imaging. Organoids were imaged by HSLCI between 6 and 48 hours after treatment. After imaging, we performed an ATP assay to assess cell viability in accordance with the manufacturer's instructions. The media was aspirated from each well and replaced with 50µL of 5 mg/mL Dispase (Thermo-Fisher) solution to digest the Matrigel. After a 25-minute incubation at 37°C, the plate was placed on an orbital shaker for 5 minutes at 80 RPM. We then added 30 µL of CellTiter-Glo® reagent (Promega), sealed the plate with film, covered the plate with foil to protect from light, shook the plate for 5 minutes at 80 RPM, and incubated at room temperature for an additional 20 minutes. We used a SpectraMax iD3 plate reader to measure luminescence. The program parameters for luminescence readings were 5 minutes of shaking prior to reading, reading all wavelengths, and integrating signal over 500ms. Organoid viability within each well was calculated by dividing the luminescent signal from each well by the mean luminescence of the control (1% DMSO) wells. Two-tailed independent t-tests were performed to assess the statistical significance of the differences in organoid mass and cell viability. P-values less than 0.05 were deemed significant.

HSLCI Data Analysis

Image processing and data analysis were performed on a downstream computer using a custom, multi-step MATLAB pipeline. First, interferograms captured by the SID4Bio QWLSI camera on one leg of the squares were converted to phase shift images using the SID4 software development kit for MATLAB (Phasics). Next, phase images are segmented into individual cells or organoids using a combination of a Gaussian lowpass filter and a watershed transform. Mass is extracted from the segmented area of each object by integrating the phase shift over that area and then multiplying by the experimentally determined specific refractive increment of 1.8×10-4 m^3/kg [25,42–45]. Finally, objects identified by image segmentation were tracked over time using a particle tracking code originally developed by John Crocker and David Grier for IDL[46], and subsequently adapted for MATLAB by Daniel Blair and Eric Dufresne.

To ensure quality of hourly growth rates recorded, data were filtered such that only biomass tracks with a 75th percentile of mass of 350pg and only segments of biomass tracks (mass vs. time) exhibiting sufficiently low local variability were included. The minimum mass filter ensures that our data does not include organoids that are already dead at the start of tracking. Variability was assessed by calculating the standard deviation of normalized mass changes within a bin of 11 mass versus time data points. The maximum allowed standard deviations were 2.8% and 3.6% for MCF-7 and BT-474, respectively. This accounts for the noise introduced by cell debris or out-of-focus objects and excludes portions of tracks if they are interrupted by debris or move out of focus. Furthermore, segments of mass versus time tracks with high local variability were fit to a sigmoidal filter and those with a goodness-of-fit better than a user-defined threshold were kept, to include tracks corresponding to cells that start alive and in focus and die over the duration of tracking.

Bibliography

1. Letai, A. Functional precision cancer medicine-moving beyond pure genomics. Nat. Med. 23, 1028–1035 (2017).

2. Bhola, P. D. et al. High-throughput dynamic BH3 profiling may quickly and accurately predict effective therapies in solid tumors. Sci. Signal. 13, (2020).

3. Phan, N. et al. A simple high-throughput approach identifies actionable drug sensitivities in patient-derived tumor organoids. Commun. Biol. 2, 1–11 (2019).

4. Vlachogiannis, G. et al. Patient-derived organoids model treatment response of metastatic gastrointestinal cancers. Science 359, 920–926 (2018).

5. Guillen, K. P. et al. A breast cancer patient-derived xenograft and organoid platform for drug discovery and precision oncology. bioRxiv 2021.02.28.433268 (2021) doi:10.1101/2021.02.28.433268.

6. Lo, Y.-H., Karlsson, K. & Kuo, C. J. Applications of organoids for cancer biology and precision medicine. Nat. Cancer 1, 761–773 (2020).

7. Ma, Y.-S. et al. The power and the promise of organoid models for cancer precision medicine with next-generation functional diagnostics and pharmaceutical exploitation. Transl. Oncol. 14, 101126 (2021).

8. Drost, J. & Clevers, H. Organoids in cancer research. Nat. Rev. Cancer 18, 407–418 (2018).

9. Marquart, J., Chen, E. Y. & Prasad, V. Estimation of the Percentage of US Patients With Cancer Who Benefit From Genome-Driven Oncology. JAMA Oncol. 4, 1093–1098 (2018).

10. Lam, S. S.-Y., He, A. B.-L. & Leung, A. Y.-H. Treatment of acute myeloid leukemia in the next decade – Towards real-time functional testing and personalized medicine. Blood Rev. 31, 418–425 (2017).

11. Friedman, A. A. et al. Feasibility of Ultra-High-Throughput Functional Screening of Melanoma Biopsies for Discovery of Novel Cancer Drug Combinations. Clin. Cancer Res. 23, 4680–4692 (2017).

12. Lee, S. H. et al. Tumor Evolution and Drug Response in Patient-Derived Organoid Models of Bladder Cancer. Cell 173, 515-528.e17 (2018).

13. Porter, R. J., Murray, G. I. & McLean, M. H. Current concepts in tumour-derived organoids. Br. J. Cancer 123, 1209–1218 (2020).

14. Schutgens, F. & Clevers, H. Human Organoids: Tools for Understanding Biology and Treating Diseases. Annu. Rev. Pathol. 15, 211–234 (2020).

15. Nguyen, H. T. L. & Soragni, A. Patient-Derived Tumor Organoid Rings for Histologic Characterization and High-Throughput Screening. STAR Protoc. 1, (2020).

16. Shihabi, A. A. et al. Personalized chordoma organoids for drug discovery studies. bioRxiv 2021.05.27.446040 (2021) doi:10.1101/2021.05.27.446040.

17. Mazzocchi, A., Soker, S. & Skardal, A. 3D bioprinting for high-throughput screening: Drug screening, disease modeling, and precision medicine applications. Appl. Phys. Rev. 6, 011302 (2019).

18. Daly, A. C., Prendergast, M. E., Hughes, A. J. & Burdick, J. A. Bioprinting for the Biologist. Cell 184, 18–32 (2021).

19. Mao, S. et al. Bioprinting of in vitro tumor models for personalized cancer treatment: a review. Biofabrication 12, 042001 (2020).

20. Kang, Y., Datta, P., Shanmughapriya, S. & Ozbolat, I. T. 3D Bioprinting of Tumor Models for Cancer Research. ACS Appl. Bio Mater. 3, 5552–5573 (2020).

21. Liu, T., Delavaux, C. & Zhang, Y. S. 3D bioprinting for oncology applications. J. 3D Print. Med. 3, 55–58 (2019).

22. Yi, H.-G. Introduction to bioprinting of in vitro cancer models. Essays Biochem. (2021) doi:10.1042/EBC20200104.

23. Huang, D. et al. High-Speed Live-Cell Interferometry: A New Method for Quantifying Tumor Drug Resistance and Heterogeneity. Anal. Chem. 90, 3299–3306 (2018).

24. Murray, G. F. et al. Live Cell Mass Accumulation Measurement Non-Invasively Predicts Carboplatin Sensitivity in Triple-Negative Breast Cancer Patient-Derived Xenografts. ACS Omega 3, 17687–17692 (2018).

25. Reed, J. et al. Rapid, Massively Parallel Single-Cell Drug Response Measurements via Live Cell Interferometry. Biophys. J. 101, 1025–1031 (2011).

26. Bon, P., Maucort, G., Wattellier, B. & Monneret, S. Quadriwave lateral shearing interferometry for quantitative phase microscopy of living cells. Opt. Express 17, 13080–13094 (2009).

27. Murray, G. et al. Application of Quantitative Phase Imaging mass accumulation measurements to research and clinical problems in cancer. in Quantitative Phase Imaging V (eds. Popescu, G. & Park, Y.) 49 (SPIE, 2019). doi:10.1117/12.2514597.

28. Murray, G. F., Guest, D., Mikheykin, A., Toor, A. & Reed, J. Single cell biomass tracking allows identification and isolation of rare targeted therapy-resistant DLBCL cells within a mixed population. The Analyst 146, 1157–1162 (2021).

29. Chun, J. et al. Rapidly quantifying drug sensitivity of dispersed and clumped breast cancer cells by mass profiling. The Analyst 137, 5495 (2012).

30. Murray, G. F. et al. QPI Allows in vitro Drug Screening of Triple Negative Breast Cancer PDX Tumors and Fine Needle Biopsies. Front. Phys. 7, 158 (2019).

31. Chen, S., Zhou, Y., Chen, Y. & Gu, J. fastp: an ultra-fast all-in-one FASTQ preprocessor. Bioinforma. Oxf. Engl. 34, i884–i890 (2018).

32. Dobin, A. et al. STAR: ultrafast universal RNA-seq aligner. Bioinformatics 29, 15–21 (2013).

33. Kim, D., Paggi, J. M., Park, C., Bennett, C. & Salzberg, S. L. Graph-based genome alignment and genotyping with HISAT2 and HISAT-genotype. Nat. Biotechnol. 37, 907–915 (2019).

34. Bray, N. L., Pimentel, H., Melsted, P. & Pachter,

L. Near-optimal probabilistic RNA-seq quantification. Nat. Biotechnol. 34, 525–527 (2016).

35. Li, B. & Dewey, C. N. RSEM: accurate transcript quantification from RNA-Seq data with or without a reference genome. BMC Bioinformatics 12, 323 (2011).

36. Shen, S. et al. rMATS: Robust and flexible detection of differential alternative splicing from replicate RNA-Seq data. Proc. Natl. Acad. Sci. 111, E5593–E5601 (2014).

37. Lo Giudice, C., Tangaro, M. A., Pesole, G. & Picardi, E. Investigating RNA editing in deep transcriptome datasets with REDItools and REDIportal. Nat. Protoc. 15, 1098–1131 (2020).

38. Haas, B. J. et al. Accuracy assessment of fusion transcript detection via read-mapping and de novo fusion transcript assembly-based methods. Genome Biol. 20, 213 (2019).

39. Nicorici, D. et al. FusionCatcher – a tool for finding somatic fusion genes in paired-end RNA-sequencing data. bioRxiv 011650 (2014) doi:10.1101/011650.

40. Uhrig, S. et al. Accurate and efficient detection of gene fusions from RNA sequencing data. Genome Res. 31, 448–460 (2021).

41. P'ng, C. et al. BPG: Seamless, automated and interactive visualization of scientific data. BMC Bioinformatics 20, 42 (2019).

42. Barer, R. & Joseph, S. Refractometry of Living Cells : Part I. Basic Principles. J. Cell Sci. s3-95, 399–423 (1954).

43. Barer, R. & Ross, K. a. F. Refractometry of living cells. J. Physiol. 118, 38P-39P (1952).

44. Ross, K. F. A. Phase Contrast and Interference Microscopy for Cell Biologists. (Edward Arnold).

45. Barer, R. Interference Microscopy and Mass Determination. Nature 169, 366–367 (1952).

46. Crocker, J. C. & Grier, D. G. Methods of Digital Video Microscopy for Colloidal Studies. J. Colloid Interface Sci. 179, 298–310 (1996).

47. Alam, A. U., Howlader, M. M. R. & Deen, M. J. The effects of oxygen plasma and humidity on surface roughness, water contact angle and hardness of silicon, silicon dioxide and glass. J. Micromechanics Microengineering 24, 035010 (2014).

48. Nair, K. et al. Characterization of cell viability during bioprinting processes. Biotechnol. J. 4, 1168–1177 (2009).

49. Boularaoui, S., Al Hussein, G., Khan, K. A., Christoforou, N. & Stefanini, C. An overview of extrusion-based bioprinting with a focus on induced shear stress and its effect on cell viability. Bioprinting 20, e00093 (2020).

50. Szymański, P., Markowicz, M. & Mikiciuk-Olasik, E. Adaptation of High-Throughput Screening in Drug Discovery—Toxicological Screening Tests. Int. J. Mol. Sci. 13, 427–452 (2011).

51. Miles, B. & Lee, P. L. Achieving Reproducibility and Closed-Loop Automation in Biological Experimentation with an IoT-Enabled Lab of the Future. SLAS Technol. Transl. Life Sci. Innov. 23, 432–439 (2018).

52. Kroll, T. et al. Molecular characterization of breast cancer cell lines by expression profiling. J. Cancer Res. Clin. Oncol. 128, 125–134 (2002).

53. Dai, X., Cheng, H., Bai, Z. & Li, J. Breast Cancer Cell Line Classification and Its Relevance with Breast Tumor Subtyping. J. Cancer 8, 3131–3141 (2017).

54. Comşa, Ş., Cîmpean, A. M. & Raica, M. The Story of MCF-7 Breast Cancer Cell Line: 40 years of Experience in Research. Anticancer Res. 35, 3147–3154 (2015).

55. Lee, A. V., Oesterreich, S. & Davidson, N. E. MCF-7 Cells—Changing the Course of Breast Cancer Research and Care for 45 Years. JNCI J. Natl. Cancer Inst. 107, (2015).

56. Ayoub, N. M., Ibrahim, D. R., Alkhalifa, A. E. & Al-Husein, B. A. Crizotinib induced antitumor activity and synergized with chemotherapy and hormonal drugs in breast cancer cells via downregulating MET and estrogen receptor levels. Invest. New Drugs 39, 77–88 (2021).

57. Bush, S. J., Chen, L., Tovar-Corona, J. M. & Urrutia, A. O. Alternative splicing and the evolution of phenotypic novelty. Philos. Trans. R. Soc. B Biol. Sci. 372, 20150474 (2017).

58. Liu, Y. et al. Impact of Alternative Splicing on the Human Proteome. Cell Rep. 20, 1229–1241 (2017).

59. Climente-González, H., Porta-Pardo, E., Godzik, A. & Eyras, E. The Functional Impact of Alternative Splicing in Cancer. Cell Rep. 20, 2215–2226 (2017).

60. Tamaoki, T. et al. Staurosporine, a potent inhibi-

tor of phospholipidCa++dependent protein kinase. Biochem. Biophys. Res. Commun. 135, 397–402 (1986).

61. Johnston, S. R. D. & Leary, A. Lapatinib: a novel EGFR/HER2 tyrosine kinase inhibitor for cancer. Drugs Today Barc. Spain 1998 42, 441–453 (2006).

62. Liston, D. R. & Davis, M. Clinically Relevant Concentrations of Anticancer Drugs: A Guide for Nonclinical Studies. Clin. Cancer Res. 23, 3489–3498 (2017).

63. Park, J. J. H., Hsu, G., Siden, E. G., Thorlund, K. & Mills, E. J. An overview of precision oncology basket and umbrella trials for clinicians. CA. Cancer J. Clin. 70, 125–137 (2020).

64. Senft, D., Leiserson, M. D. M., Ruppin, E. & Ronai, Z. A. Precision Oncology: The Road Ahead. Trends Mol. Med. 23, 874–898 (2017).

65. Schwartzberg, L., Kim, E. S., Liu, D. & Schrag, D. Precision Oncology: Who, How, What, When, and When Not? Am. Soc. Clin. Oncol. Educ. Book 160–169 (2017) doi:10.1200/EDBK_174176.

66. Morgan, G., Aftimos, P. & Awada, A. Current-day precision oncology: from cancer prevention, screening, drug development, and treatment – have we fallen short of the promise? Curr. Opin. Oncol. 28, 441–446 (2016).

67. Kane, K. I. W. et al. Determination of the rheological properties of Matrigel for optimum seeding conditions in microfluidic cell cultures. AIP Adv. 8, 125332 (2018).

68. Zangle, T. A., Teitell, M. A. & Reed, J. Live Cell Interferometry Quantifies Dynamics of Biomass Partitioning during Cytokinesis. PLoS ONE 9, e115726 (2014).

69. Reed, J. et al. Live Cell Interferometry Reveals Cellular Dynamism During Force Propagation. ACS Nano 2, 841–846 (2008).

70. Reed, J. et al. High throughput cell nanomechanics with mechanical imaging interferometry. Nanotechnology 19, 235101 (2008).

71. Ledwig, P. & Robles, F. E. Epi-mode tomographic quantitative phase imaging in thick scattering samples. Biomed. Opt. Express 10, 3605–3621 (2019).

72. Martelotto, L. G., Ng, C. K., Piscuoglio, S., Weigelt, B. & Reis-Filho, J. S. Breast cancer intra-tumor heterogeneity. Breast Cancer Res. 16, 210 (2014).

73. Stanta, G. & Bonin, S. Overview on Clinical Relevance of Intra-Tumor Heterogeneity. Front. Med. 5, (2018).

74. Dentro, S. C. et al. Characterizing genetic intra-tumor heterogeneity across 2,658 human cancer genomes. Cell 184, 2239-2254.e39 (2021).

75. Espiritu, S. M. G. et al. The Evolutionary Landscape of Localized Prostate Cancers Drives Clinical Aggression. Cell 173, 1003-1013.e15 (2018).

76. Somasundaram, R., Villanueva, J. & Herlyn, M. Chapter Eleven - Intratumoral Heterogeneity as a Therapy Resistance Mechanism: Role of Melanoma Subpopulations. in Advances in Pharmacology (ed. Smalley, K. S. M.) vol. 65 335–359 (Academic Press, 2012).

77. Auffinger, B., Spencer, D., Pytel, P., Ahmed, A. U. & Lesniak, M. S. The role of glioma stem cells in chemotherapy resistance and glioblastoma multiforme recurrence. Expert Rev. Neurother. 15, 741–752 (2015).

78. Lacerda, L., Pusztai, L. & Woodward, W. A. The role of tumor initiating cells in drug resistance of breast cancer: Implications for future therapeutic approaches. Drug Resist. Updat. 13, 99–108 (2010).

Supplementary Material

High-speed live cell interferometry for screening bioprinted organoids

Peyton J. Tebon*, Bowen Wang*, Alexander L. Markowitz, Graeme Murray, Huyen Thi Lam Nguyen, Nasrin Tavanaie, Thang L. Nguyen, Paul C. Boutros, Michael A. Teitell[#] and Alice Soragni[#]

Supplementary Videos

Supplementary Video 1. MCF-7 organoids treated with the vehicle control. Scan the QR code to access the video or visualize at the following link: https://youtu.be/bUBq-ZChFM0

Supplementary Video 2. BT-474 organoids treated with the vehicle control. Scan the QR code to access the video or visualize at the following link: https://youtu.be/AzSc8WW5KBA

Supplementary Tables

A

				Organoid Behavior (%)		
MCF-7		Time (h)	n	Gained Mass	Stable	Lost Mass
Vehicle	1% DMSO	12	93	20.4	74.2	5.4
		24	109	36.7	51.4	11.9
		48	89	37.1	42.7	20.2
Staurosporine	0.1 μM	12	34	8.8	76.5	14.7
		24	43	16.3	60.5	23.3
		48	34	29.4	38.2	32.4
	1 μM	12	28	7.1	82.1	10.7
		24	28	3.6	71.4	25.0
		48	30	0.0	73.3	26.7
	10 μM	12	49	2.0	79.6	18.4
		24	37	0.0	51.4	48.6
		48	28	3.6	32.1	64.3
Lapatinib	0.1 μM	12	34	17.6	73.5	8.8
		24	32	28.1	56.3	15.6
		48	32	46.9	34.4	18.8
	1 μM	12	34	8.8	88.2	2.9
		24	31	45.2	45.2	9.7
		48	38	55.3	26.3	18.4
	10 μM	12	44	6.8	84.1	9.1
		24	46	26.1	56.5	17.4
		48	37	32.4	32.4	35.1
	50 μM	12	29	6.9	58.6	34.5
		24	28	14.3	39.3	46.4
		48	23	4.3	43.5	52.2

B

BT-474		Time (h)	n	Organoid Behavior (%)		
				Gained Mass	Stable	Lost Mass
Vehicle	1% DMSO	12	125	31.2	65.6	3.2
		24	136	61.8	33.1	5.1
		48	106	82.1	16.0	1.9
Staurosporine	0.1 μM	12	58	27.6	70.7	1.7
		24	72	45.8	50.0	4.2
		48	77	70.1	23.4	6.5
	1 μM	12	42	19.0	47.6	33.3
		24	44	13.6	29.5	56.8
		48	25	4.0	12.0	84.0
	10 μM	12	42	7.1	64.3	28.6
		24	46	19.6	23.9	56.5
		48	27	14.8	18.5	66.7
Lapatinib	0.1 μM	12	64	28.1	68.8	3.1
		24	57	49.1	45.6	5.3
		48	31	67.7	25.8	6.5
	1 μM	12	54	14.8	77.8	7.4
		24	59	20.3	54.2	25.4
		48	40	27.5	50.0	22.5
	10 μM	12	56	19.6	73.2	7.1
		24	63	9.5	60.3	30.2
		48	53	15.1	47.2	37.7
	50 μM	12	65	13.8	67.7	18.5
		24	72	9.7	55.6	34.7
		48	26	3.8	11.5	84.6

Table S1. Proportions of organoids that gained, lost, and maintained mass by treatment condition. (A) Proportions of MCF-7 organoids. (B) Proportions of BT-474 organoids. Data is plotted in Figure S6.

A

		6 hours		48 hours	
MCF-7		Mean mass ± SD	p-value	Mean mass ± SD	p-value
Vehicle	1% DMSO	2.07 ± 1.25		2.48 ± 1.89	
Staurosporine	0.1 μM	1.71 ± 0.92	0.6638	1.68 ± 1.05	0.1375
	1 μM	1.77 ± 1.34	0.8949	1.33 ± 1.08	0.0121
	10 μM	1.63 ± 0.83	0.3653	1.26 ± 0.80	0.0086
Lapatinib	0.1 μM	2.00 ± 1.46	0.9997	2.76 ± 2.39	0.9713
	1 μM	2.20 ± 1.36	0.9978	2.71 ± 2.12	0.9887
	10 μM	2.30 ± 1.51	0.9439	2.46 ± 1.93	>0.9999
	50 μM	1.71 ± 0.86	0.8748	1.32 ± 1.06	0.0285

B

		6 hours		48 hours	
BT-474		Mean mass ± SD	p-value	Mean mass ± SD	p-value
Vehicle	1% DMSO	1.62 ± 0.57		2.36 ± 1.02	
Staurosporine	0.1 μM	1.63 ± 0.85	0.9999	2.12 ± 1.06	0.4334
	1 μM	1.38 ± 0.49	0.7766	0.70 ± 0.26	<0.0001
	10 μM	1.46 ± 0.72	0.9412	0.83 ± 0.72	<0.0001
Lapatinib	0.1 μM	1.84 ± 1.21	0.5339	2.33 ± 1.58	0.9998
	1 μM	1.58 ± 0.78	0.9997	1.48 ± 0.66	<0.0001
	10 μM	1.74 ± 0.88	0.9476	1.42 ± 0.75	<0.0001
	50 μM	1.58 ± 0.70	0.9997	0.92 ± 0.48	<0.0001

Table S2. Means, standard deviations, and p-values from independent, two-tailed t-tests. In all figures, $p<0.05$ is denoted by *, $p<0.01$ is denoted by **, and $p<0.001$ is denoted by ***. (A) Comparisons of mean mass of MCF-7 organoids calculated via HSLCI. P-values are calculated by comparing each experimental condition (n=8 staurosporine, n=3 lapatinib) to the vehicle control (n=12) at the respective time point. Data is presented in Figure 6B. (B) Comparisons of mean mass of BT-474 organoids calculated via HSLCI. The p-values are calculated by comparing each experimental condition (n=7 staurosporine, n=6 lapatinib) to the vehicle control (n=12) at the respective time point. Data is presented in Figure 6B. (C) Comparisons of cell viability measured by ATP assay. Data is presented in Figure 6E.

		MCF-7		BT-474	
		Viability ± SD	p-value	Viability ± SD	p-value
Vehicle	1% DMSO	1.00 ± 0.21		1.00 ± 0.20	
Staurosporine	0.1 μM	0.50 ± 0.08	<0.0001	0.58 ± 0.14	0.0002
	1 μM	0.17 ± 0.04	<0.0001	0.02 ± 0.01	<0.0001
	10 μM	0.13 ± 0.03	<0.0001	0.01 ± 0.00	<0.0001
Lapatinib	0.1 μM	1.00 ± 0.03	0.9452	0.70 ± 0.18	0.0113
	1 μM	1.01 ± 0.04	0.8598	0.43 ± 0.09	<0.0001
	10 μM	0.66 ± 0.07	0.0018	0.32 ± 0.04	<0.0001
	50 μM	0.14 ± 0.03	<0.0001	0.09 ± 0.07	<0.0001

Table S3. Organoid viability analysis by endpoint ATP assay. Comparisons of cell viability measured by ATP assay. P-values calculated by unpaired t-test with Welch's correction. Data is presented in Figure 6E.

Supplementary Figures

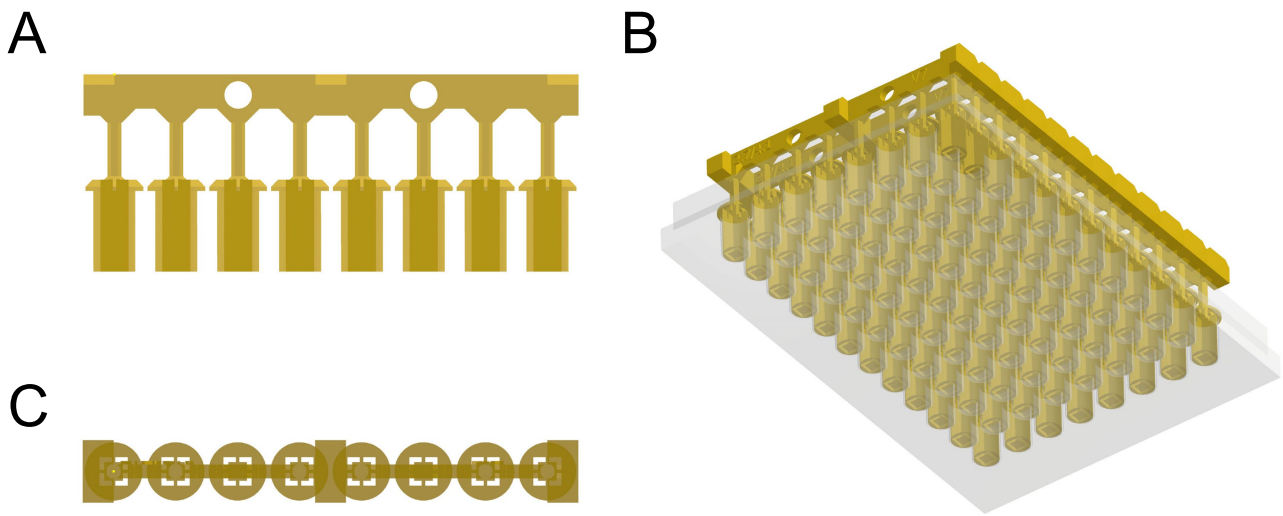

Figure S1. Schematics of well mask. (A) Side view. (B) Bottom view. (C) Plasma masks inserted into 96-well plate viewed from bottom.

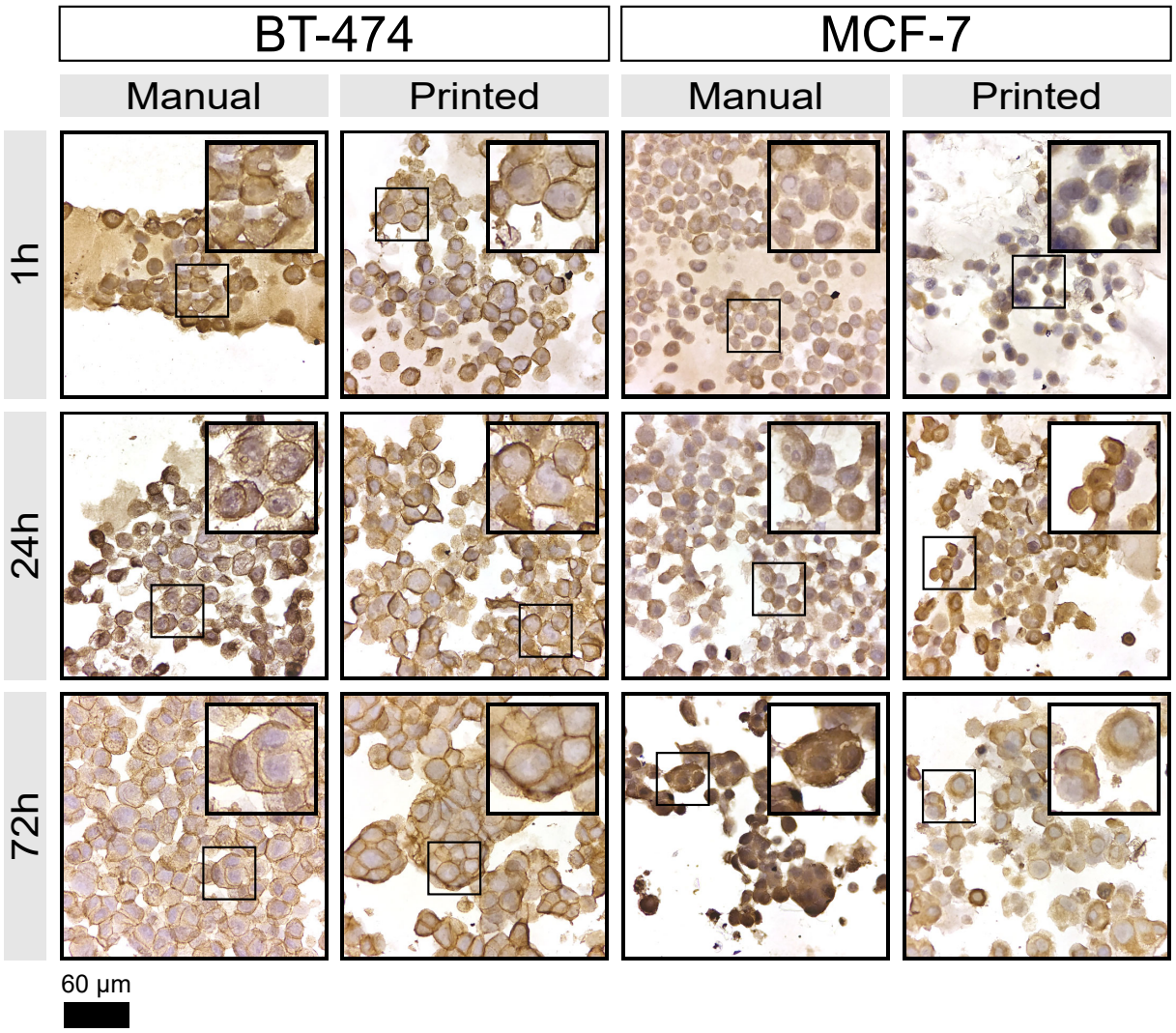

Figure S2. HER2 expression in BT-474 and MCF-7 organoids. Immunohistochemistry staining of 3D cultures for HER2. BT-474 cells have amplified HER2 expression[53,56] while MCF-7 cells express lower levels of HER2 and lack HER2 amplification[53–55].

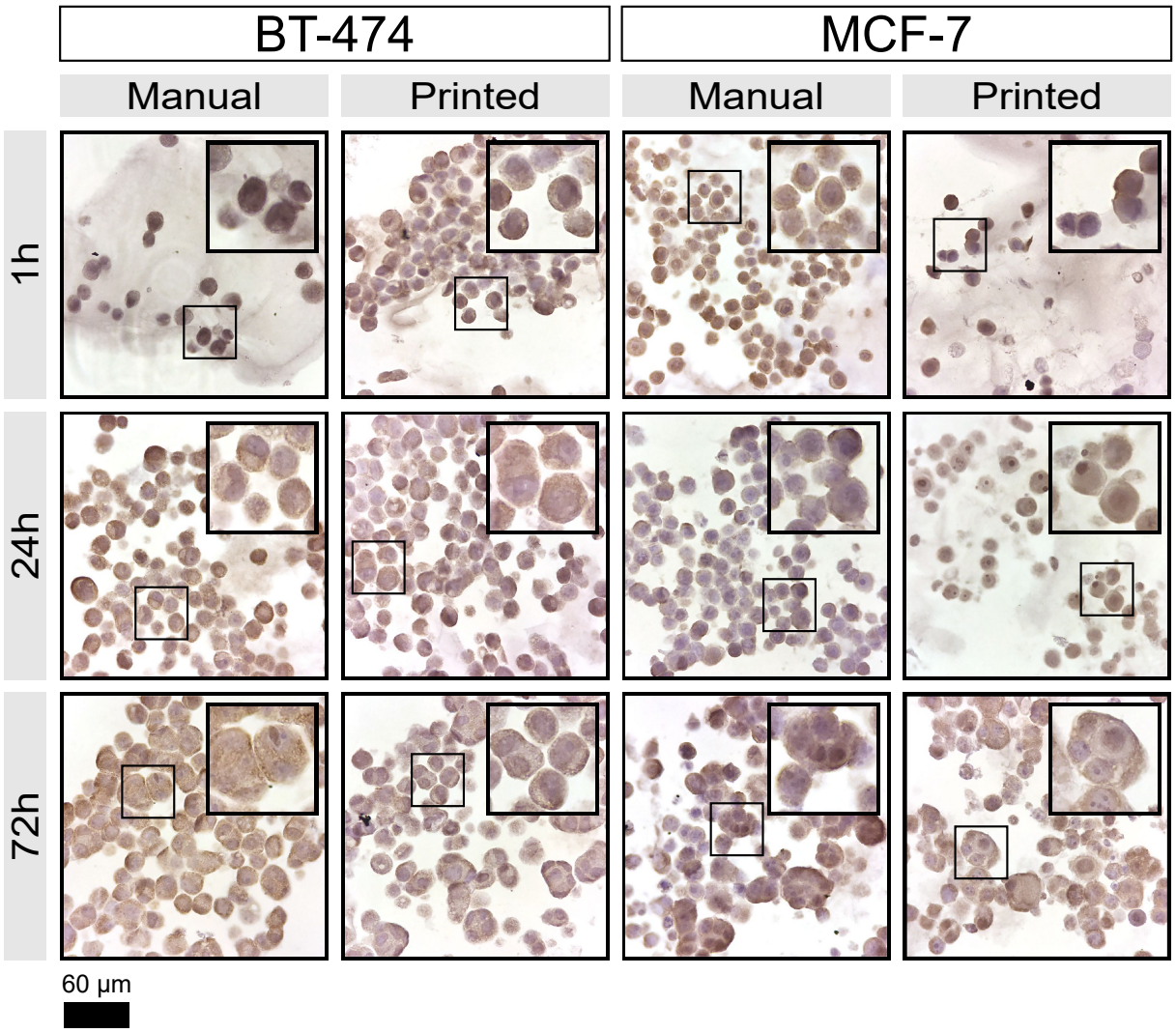

Figure S3. Estrogen Receptor Expression in BT-474 and MCF-7 organoids. Immunohistochemistry staining of 3D cultures for ER. Both BT-474 and MCF-7 cell lines are ER-positive[53–56].

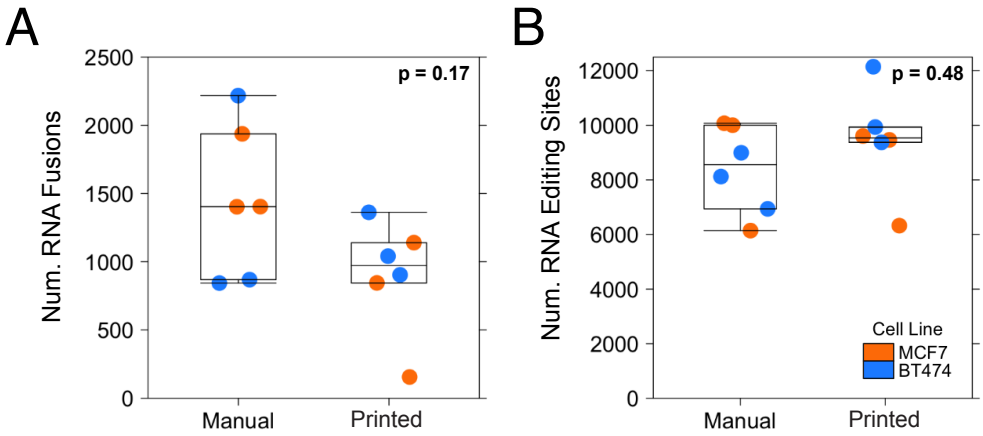

Figure S4. RNA Fusions and Editing Sites. (A) Number of RNA fusions detected by FusionCatcher by tumor organoid seeding method. The number of RNA fusions did not significantly differ between manually seeded and bioprinted organoids ($p_{BT\text{-}474} = 0.179$, $p_{MCF\text{-}7} = 0.179$). (B) The number of adenosine-to-inosine (A-to-I) RNA editing sites detected by REDItools were not associated with tumor organoid development method ($p = 0.48$, Mann-Whitney U-test). By cell line, the number of A-to-I RNA editing sites did not differ between printed and manually seeded organoids ($p_{BT\text{-}474} = 0.1$, $p_{MCF\text{-}7} = 0.7$).

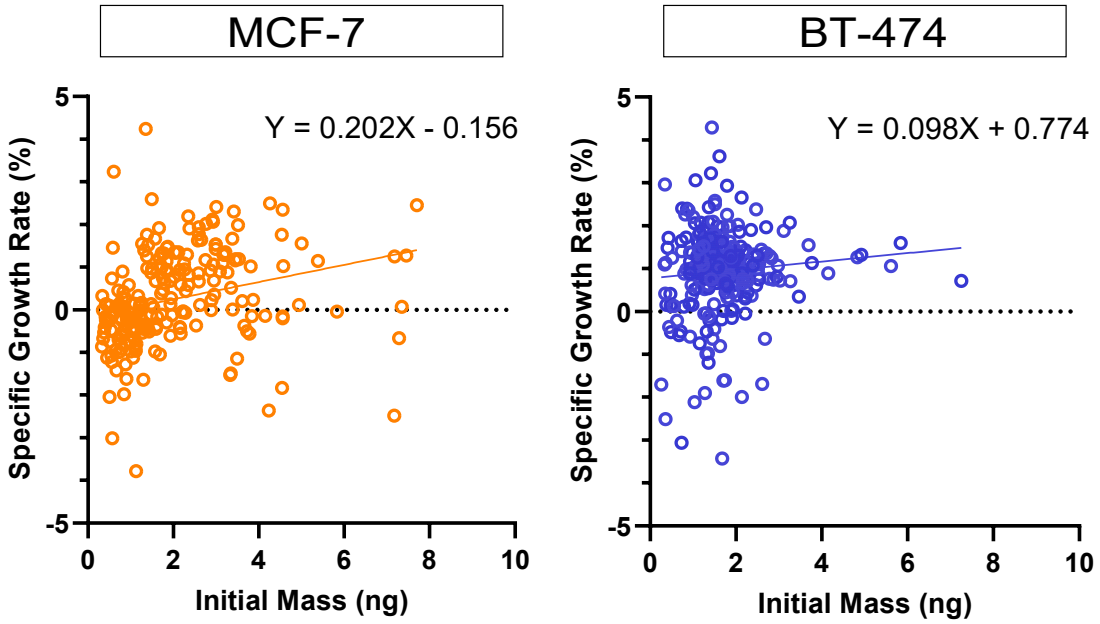

Figure S5. Specific growth rate correlates to initial organoid mass. Specific growth rate (growth in mass as a percentage of total mass) versus initial organoid mass was plotted for all organoids tracked. Linear regression analysis showed a significant positive relationship between initial organoid mass and specific growth rate for MCF=7 organoids (95% confidence interval of slope is 0.1040 to 0.2993), but not for BT-474 organoids (95% CI of slope -0.041 to 0.2363).

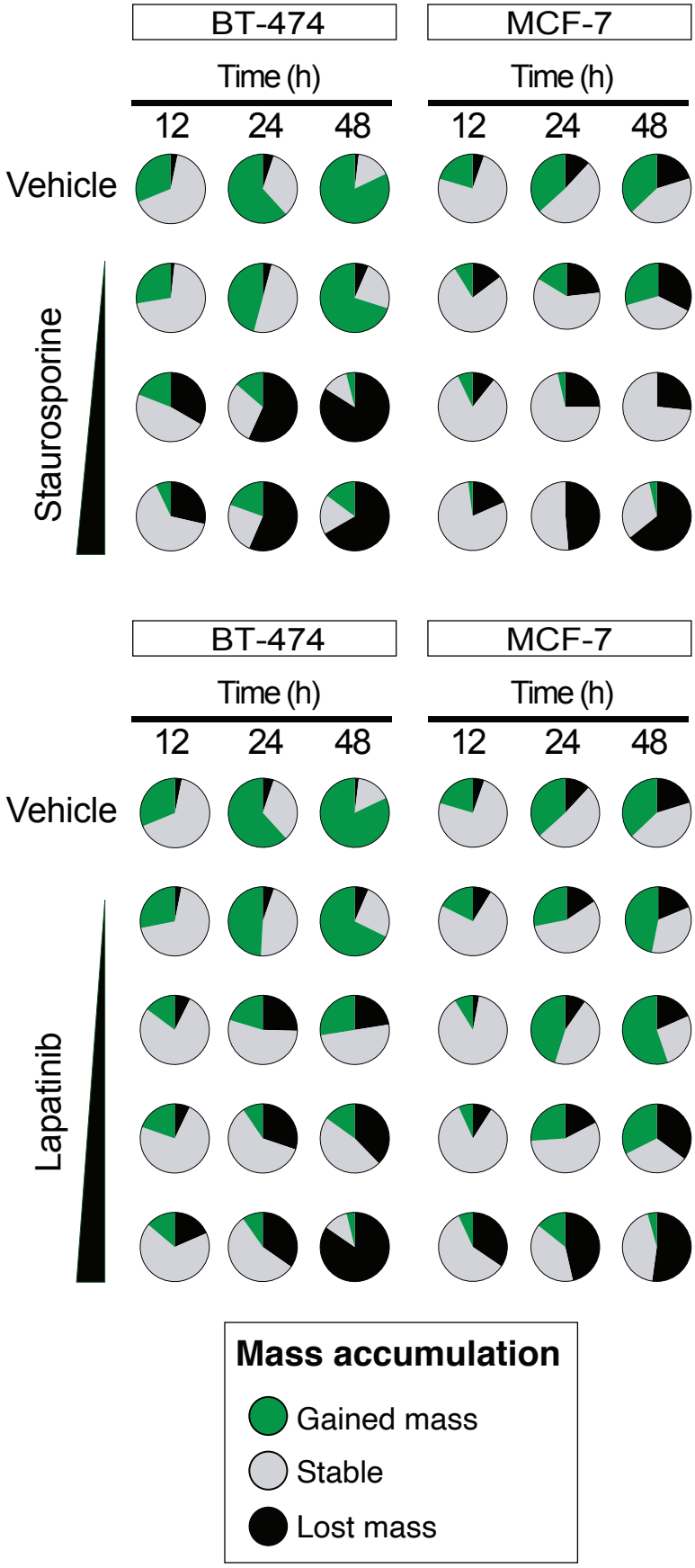

Figure S6. Categorization of organoid mass change. Pie charts displaying the proportion of organoids that had gained mass (mass increase by >10%), remained stable (mass change <10%), or lost mass (mass loss of >10%) after 12, 24, and 48 hours.